JOURNAL OF GEOPHYSICAL RESEARCH, VOL. 96, NO. B7, PAGES 11,831–11,848, JULY 10, 1991

The Equation of State of a Molten Komatiite 1. Shock Wave Compression to 36 GPa

GREGORY H. MILLER,[1,2] EDWARD M. STOLPER, AND THOMAS J. AHRENS[1]

Division of Geological and Planetary Sciences, California Institute of Technology, Pasadena

The equation of state (EOS) of an initially molten (1550°C) komatiite (27 wt % MgO) was determined in the 5-36 GPa pressure range via shock wave compression. Shock wave velocity U_s and particle velocity U_p (kilometers/second) follow the linear relationship $U_s = 3.13(\pm0.03) + 1.47(\pm0.03)\ U_p$. Based on a calculated density at 1550°C, 0 bar of 2.745±0.005 g/cm^3, this U_s–U_p relationship gives the isentropic bulk modulus $K_S = 27.0 \pm 0.6$ GPa, and its first and second isentropic pressure derivatives, $K'_S = 4.9 \pm 0.1$ and $K''_S = -0.109 \pm 0.003$ GPa^{-1}. The calculated liquidus compression curve agrees within error with the static compression results of Agee and Walker (1988) to 6 GPa but is less dense than their extrapolated values at higher pressures. We determine that olivine (Fo_{94}) will be neutrally buoyant in komatiitic melt of the composition that we studied near 8.2 GPa. Clinopyroxene would also be neutrally buoyant near this pressure. Liquidus garnet-majorite may be less dense than this komatiitic liquid in the 20-24 GPa interval; however, pyropic-garnet and perovskite phases are denser than this komatiitic liquid in their respective liquidus pressure intervals to 36 GPa. Liquidus perovskite may be neutrally buoyant near 70 GPa. At 40 GPa, the density of shock-compressed molten komatiite would be approximately equal to the calculated density of an equivalent mixture of dense solid oxide components. This observation supports the model of Rigden et al. (1989) for compressibilities of liquid oxide components. Using their theoretical EOS for liquid forsterite and fayalite, we calculate the densities of a spectrum of melts from basaltic through peridotitic that are related to the experimentally studied komatiitic liquid by addition or subtraction of olivine. At low pressure, olivine fractionation lowers the density of basic magmas, but above 13-14 GPa this trend is reversed. All of these basic to ultrabasic liquids are predicted to have similar densities at 13-14 GPa, and this density is approximately equal to the density of the bulk (preliminary reference Earth model) mantle in this pressure range. This suggests that melts derived from a peridotitic mantle may be inhibited from ascending from depths greater than 400 km.

1. INTRODUCTION

The pressure-volume-temperature (PVT) equation of state (EOS) of silicate melts at pressures of several tens to hundreds of kilobars has recently become an area of considerable interest. This interest stems in part from the recognition that magmatic activity extending over much of the depth of the upper mantle and perhaps even the lower mantle may have played a significant role in the early evolution and differentiation of the Earth. If so, knowledge of the equation of state would be of fundamental importance in setting constraints on the consequences of such deep-seated igneous activity. In particular, it has been suggested [*Stolper et al.*, 1981; *Nisbet and Walker*, 1982; *Rigden et al.*, 1984; *Ohtani*, 1985; *Takahashi*, 1986; *Agee and Walker*, 1987] that at sufficiently high pressures, silicate melts could become so dense that usual crystal-melt segregation (crystals sinking) would be impeded. This could result in a maximum depth from which melts could rise and could have the important consequence of burying heat and incompatible elements that might otherwise have reached the Earth's surface. In extreme cases, silicate melts could be denser than surrounding mantle rocks, resulting in a downward segregation of melts, heat, and heat-producing elements, quite the opposite of most modern shallow igneous activity.

Rigden et al. [1984, 1988] determined the EOS of a model basalt to 340 kbar and verified that silicate melts can be of comparable density to mantle minerals and rocks at high pressures. The requisite pressures (≥6 GPa) are, however, much greater than those at which basaltic magmas are generally believed to have formed [*Green and Ringwood*, 1967]. Melts generated at such high pressures are believed to be more olivine-normative than common basaltic magmas. Komatiitic liquids are examples of magmas that may originate at the high pressures at which silicate magmas may be comparable in density to olivine-rich residual materials. Recent high-pressure melting experiments [*Takahashi and Scarfe*, 1985; *Scarfe and Takahashi*, 1986] have demonstrated that liquids similar to komatiitic magmas can be generated by partial melting of garnet lherzolite at pressures of 5-7 GPa. At higher pressures, partial melting of garnet lherzolite produces even more olivine-rich magmas, approaching mantle-derived lherzolites in composition at ≈14 GPa [*Scarfe and Takahashi*, 1986]. Large-scale melting of the mantle may have occurred during accretion [*Kaula*, 1979; *Abe and Matsui*, 1986; *Matsui and Abe*, 1986; *Zahnle et al.*, 1988; *Ahrens*, 1990] or impact formation of the Moon [*Benz et al.*, 1986, 1987; *Cameron and Benz*, 1989; *Stevenson*, 1989], perhaps generating a komatiitic or peridotitic magma ocean extending to great depth. The equations of state of ultrabasic liquids are critical for evaluating hypotheses for the generation of komatiitic liquids and for quantitative evaluation of early magmatic evolution that may have extended to great depths in the Earth.

Extrapolation of the high-pressure EOS of a model basalt [*Rigden et al.*, 1984, 1988] and simple mineral melts [*Rigden et al.*, 1989] to more olivine-normative compositions involves considerable uncertainty. In particular, liquid olivine components are believed to have a relatively large isentropic bulk modulus

[1] Also at Helen E. Lindhurst Laboratory of Experimental Geophysics, California Institute of Technology, Pasadena.

[2] Now at Department of Geology and Geophysics, University of California, Berkeley.

Copyright 1991 by the American Geophysical Union.

Paper number 91JB01204.
0148-0227/91/91JB-01204$05.00

(K_S) to 100 kbar but their detailed behavior is unknown (e.g., high K_{0S} and low $\partial K_S/\partial P|_S$ (K'_{0S}) versus low K_{0S} and high K'_{0S}) and can make a big difference in extrapolation of density above a few tens of kilobars [*Rivers*, 1985; *Herzberg*, 1987]. Furthermore, although 1-bar bulk moduli of basic and ultrabasic liquids can be modeled with reasonable accuracy [*Lange and Carmichael*, 1987; *Rivers and Carmichael*, 1987] their extrapolation to 100-kbar pressures is complicated by the fact that the form of the EOS cannot be anticipated [*Rigden et al.*, 1988].

Direct high-pressure experimentation on ultrabasic liquids is required, e.g., the static compression experiments of *Agee and Walker* [1988]. Another direct experimental method for the determination of high-pressure, high-temperature liquid equations of state is shock wave compression. Shock wave compression has previously been used to measure the EOS of silicate liquids in the system anorthite-diopside to pressures of 400 kbar [*Rigden et al.*, 1984, 1988, 1989]. These results are both consistent with available low-pressure compressibility data and extend these data to lower mantle pressures through direct measurement. In this paper, we report the results of a study of the equation of state of molten komatiite to 360 kbar using shock wave techniques. This is the first report of the EOS of a complex, naturally occurring melt composition to these pressures.

The results of the high-pressure komatiite EOS are used as a basis for evaluating models of the petrogenesis of komatiitic magmas and the early evolution of the mantle in a companion paper [*Miller et al.*, this issue].

2. EXPERIMENTAL METHOD

Although the molten silicate shock wave experiment was described by *Rigden et al.* [1988], we have made some modifications to both the experimental procedure and method of data analysis. We therefore will describe the entire experimental and analytical procedure, placing emphasis on those aspects that differ from the earlier work.

A synthetic komatiite (glass plus approximately 10% spinifex olivine) was prepared at Corning Technical Center, Corning, New York, by G. Fine. The nominal composition (Table 1) was based on a natural komatiite from the Pike Hill area of Munro Township, Ontario [*Walker et al.*, 1977]. Batches of 200-g spectroscopic grade oxides were mixed, then melted at 1650°C for 4 hours in a Fe-saturated Pt crucible in air. The liquid was then poured onto a 6 by 6 inch cold steel slab to make a patty of appropriate thickness (≈ 0.5 cm) for the shock wave sample assembly. The liquid could not be quenched rapidly enough to prevent growth of spinifex olivines, but by pouring slabs of similar thickness to our sample assembly we were able to ensure that the bulk composition used in our experiments was similar to the nominal composition listed in Table 1 despite the chemical stratification of the slab. Cores of 1-cm diameter were cut from the slabs with a water-cooled diamond coring bit. The sample size was determined by a calculation of the mass of melt needed to fill 85-90% of the Mo container (see below) at 1550°C. The measured volume of the Mo sample container, corrected to 1550°C [*Touloukian et al.*, 1970], and the estimated melt density at 1550°C [*Lange and Carmichael*, 1987] determined the mass of sample needed to fill the container. The 10-15% underfilling was considered necessary to prevent rupturing or distortion of the container. The cores were ground to the desired size with 60-μm alumina.

Two cores, prepared as described above, were used to verify that the core preparation procedure did not bias the sample composition. Thin sections were cut along the axis of the cylindrical cores and analyzed with the Caltech JEOL electron microprobe. Vertical and horizontal transects across the sections were probed at approximately 50-μm intervals. Averages are presented in Table 1, column 2.

Molybdenum sample containers were machined of high purity sintered Mo stock (grade ABL-2 from Climax Specialty Metals, Coldwater, Michigan) according to the specifications of *Rigden et al.* [1988]. The inner surfaces of the container were polished to 0.3 μm with alumina to minimize the possibility of bubble adhesion and to provide a smooth and nominally flat metal/liquid interface. Some curvature of the Mo was introduced by the polishing, however, resulting in a slightly concave surface; the thickness of the Mo driver plate (Figure 1) was found to vary by 10-50 μm between the perimeter of the sample well and the center. Other dimensions of the Mo container (measured with ±1-μm precision) were the thickness of the driver plate outside of the sample well and the sample well depth and diameter. The density of the Mo container was determined to ±0.02% by the Archimedean method. The measured density agreed with the published density [*Straumanis and Shodhan*, 1968] within the reported errors, confirming negligible porosity and impurities. A Mo cover was machined to fit the sample container. The inner surface of the cover was lapped to 0.3 μm, and its thickness was measured to ±1 μm. The lapping produced no measurable curvature. The komatiite cores were

TABLE 1. Experimental Komatiite Composition

Oxide	Nominal	Measured[a]	Measured After Heating in Mo Container[a]
SiO_2	46.1	45.4	46.5
MgO	27.2	26.6	27.7
FeO[b]	9.7	8.6	8.5
CaO	7.4	7.8	7.7
Al_2O_3	7.6	8.2	8.0
Na_2O	0.9	1.1	0.9
TiO_2	0.4	0.4	0.4
Cr_2O_3	0.4	0.4	0.3
K_2O	0.2	0.3	0.2
MnO	0.1	NA	NA
MoO_2	—	0.0	0.9
Total	100.0	98.8	101.1

In weight percent.

[a] Average of approximately 100 analyses obtained at 50-μm intervals along horizontal and vertical transects across the sample.

[b] All Fe calculated as FeO.

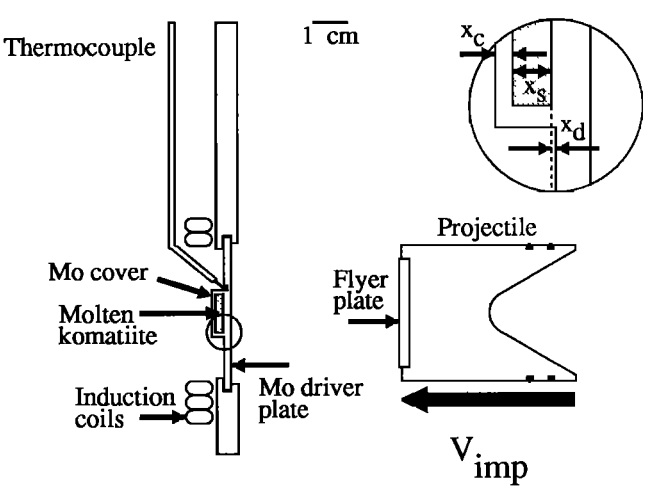

Fig. 1. Schematic of shock wave sample assembly.

placed in the Mo container, the Mo cover was seated in place, and the cover was electron beam welded at 400°C in vacuo. The heating under vacuum facilitates the electron beam welding and has the added likely benefit of driving off volatiles adsorbed on the glass. After welding, the sample assembly was measured to ensure that the cap was seated properly. Canting of the cap was checked by measurement of the thickness of the assembly across the cap to ±1 μm. The caps were found to be canted by less than 5 μm across their 1-cm diameter.

The welded sample assembly was hung vertically in a vertical tube furnace at 1500°C for 15-20 min to verify weld integrity. The liquidus temperature of the sample is approximately 1465°C, so the sample was completely melted. A continuous flow of dry N_2 gas was maintained in the furnace to minimize oxidation of the Mo. The dimensions of the sample container were measured after heating to verify that the cap was not distended from overfilling of the sample container. The loss of thickness owing to Mo loss on oxidation was less than 5 μm. One sample was cut open and examined to verify that the sample had been completely melted. Before heating, the sample consisted of spinifex olivines in a glass matrix. After heating at 1500°C, all of the spinifex olivines were replaced by uniformly distributed ≈10 μm equant skeletal olivine crystals. This textural change indicates complete melting. The sample was also examined to determine whether or not all bubbles had risen to the top of the assembly. Some bubbles persisted at the corners between the cylindrical wall and the flat surfaces of the Mo container, but the majority of the vapor phase had accumulated at the top of the container. This sample was checked for Mo contamination and Fe loss with the Caltech electron probe (Table 1, column 3).

The top surfaces of the welded sample assemblies were mirror polished with 0.3-μm alumina. Polishing made the cover measurably concave, with the center depressed up to 20 μm relative to the perimeter. The cover and driver plate thicknesses were measured to ±1 μm to determine the concavity and the thickness change during polishing. A 1.4-mm-diameter, 1-mm-deep well was drilled into the driver plate immediately adjacent to the sample chamber, and a Pt-Rh (type S) thermocouple was pressed into the well. The Mo container was then fitted into a machinable Al_2O_3 ceramic (Zircar) plate and aligned with a water-cooled pie-shaped induction coil made from Cu tubing. The sample assembly and induction coil were then aligned in the sample tank of the Caltech 40-mm propellant gun [*Ahrens et al.*, 1971]. A schematic illustration of the sample assembly and induction coil is shown in Figure 1.

The gun barrel and sample tank were evacuated to below 100 μm Hg, then the Mo sample assembly was induction-heated to 1550°C for ≈1 min. The sample was then allowed to cool to 800°C and the assembly was viewed through a glass port in the tank to verify that the capsule had not ruptured. The sample assembly was subsequently reheated to 1550°C. The sample was maintained at 1550°C for 10-20 min until the gun was fired.

The shock experiments consist of impacting the sample assembly with a metallic "flyer plate" attached to a Lexan projectile. The projectile is propelled in the evacuated gun with up to 500 g of nitroglycerine-nitrocellulose propellant to velocities up to 2.5 km/s. The projectile velocity is measured with a double-exposure 30-ns X ray shadowgraph just prior to impact. Analysis of this X ray record [e.g., *Rigden et al.*, 1988] determines the projectile velocity to within 2%.

Prior to impact, a xenon flash lamp illuminates the polished surface of the sample assembly. A streak camera is used to measure the intensity of light reflected from the sample assembly along one spatial dimension as a function of time. The spatial axis is normally positioned horizontally across the center of the sample assembly. Its field of view encompasses the Mo cover and the Mo driver plate on either side of the sample well. We use this instrument to record relative shock wave arrival times between the driver plate surface and the cover surface by detecting when the reflectivity of each surface changes. Free surfaces are empirically found to change their reflectivity when the shock wave arrives. This change could be associated with roughening due to differential rotation of grains on the surface of the polycrystalline material. Unfortunately, the 1550°C Mo surface does not show appreciable roughening by low-pressure shocks. Moreover, the impedance mismatch between Mo and molten silicate attenuates the strength of the shock, and the Mo cap experiences a lower-pressure shock than does the Mo driver. Consequently, several of our streak camera records were so difficult to interpret, particularly in the cap region, that these data were rejected.

As noted above, we necessarily had a "bubble" in the sample chamber. Most of the vapor was found to accumulate at the top of the container that was cut open after heating to 1500°C. Aside from cutting open the containers, however, we had no method of determining the location of the bubble at 1550°C in each sample assembly we wished to shock. The possible presence of a bubble in the center of the sample is of great concern since a bubble would delay the shock wave, resulting in an erroneous shock wave velocity measurement. The curvature of the shock wave arrival (discussed below), measured along the centered horizontal slit of the streak camera, could indicate the presence of a bubble in the center of the molten sample. However, the curvature could also be due to edge effects and the concavity of the polished Mo surfaces.

One approach to determining if a bubble rose to the top of the assembly is to try to detect its presence at the top of the sample by using a vertically positioned streak camera slit. We reasoned that a vertical-slit streak record would be strongly asymmetric if a bubble were present at the top of the assembly. To use a vertical slit, it was necessary to rotate the reflected vertical image through 90° with a set of three right-angle prisms onto the horizontal slit of the stationary streak camera. We conducted four experiments with this vertical-slit configuration. A schematic illustration of the vertical-slit streak camera records, and a comparison to horizontal-slit streak records is shown in Figure 2. In all cases a pronounced asymmetry was evident in the vertical-slit records. Furthermore, the vertical extent of the bubble's influence never extended beyond the center of the sample. The absence of bubble-induced delay below the centerline of the vertical-slit experiments strongly suggests that the horizontal-slit experiments are free from any bubble influence. The vertical-slit streak records below the centerline were not perfectly flat but resembled the horizontal slit records. This allowed us to associate the observed curvature of some horizontal streak records with edge effects and the effects of surface curvature.

Interpretation of Streak Records

The horizontal-slit streak record of shot 753 is reproduced in Figure 3. The time axis is horizontal on the figure, increasing from left to right, and the spatial dimension is vertical. This streak record illustrates a number of features found in some of these experiments and our interpretation of them. The streak record appears in three parts: the left side of the driver plate,

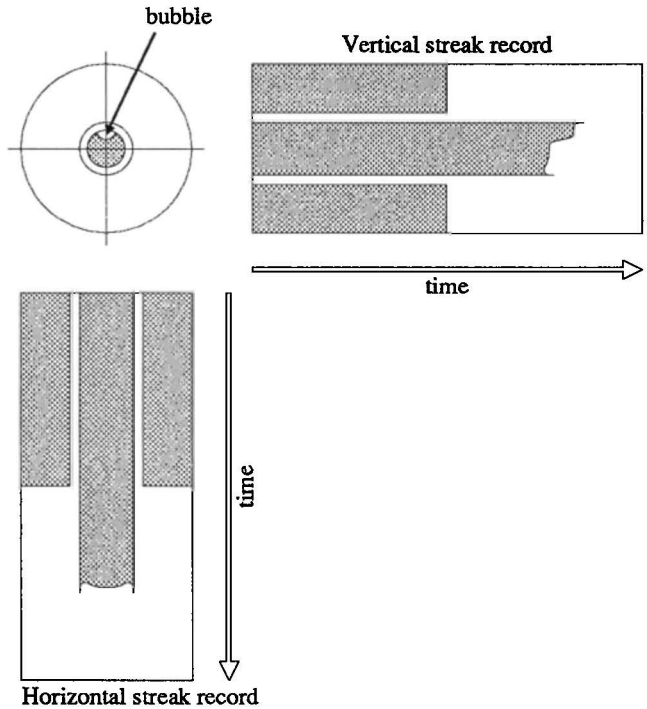

Fig. 2. Schematic horizontal- and vertical-slit streak camera records. The records show the arrival of the shock wave on the driver plate free surface.

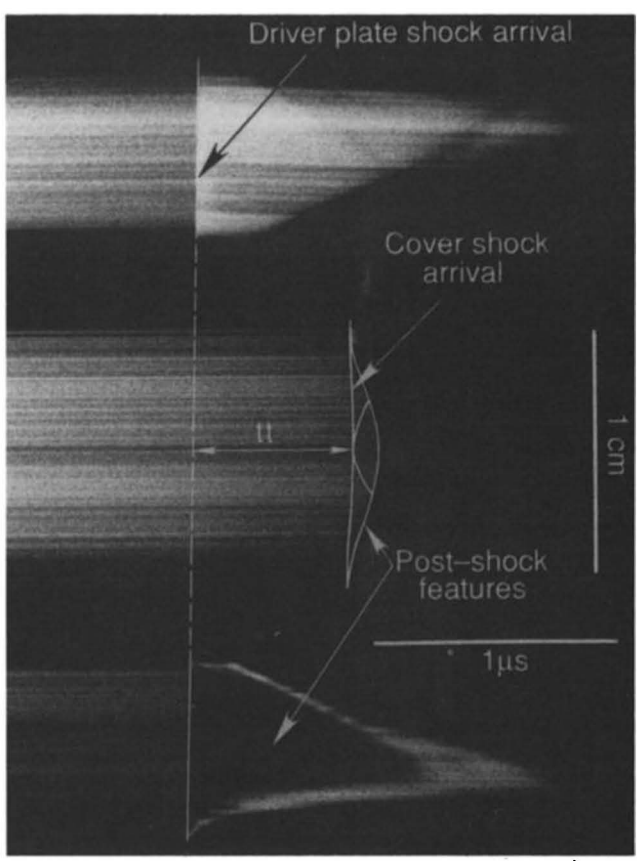

Fig. 3. The horizontal-slit streak camera record from shot 753. Reflected light along the horizontal spatial dimension (vertical axis on the figure) is recorded as a function of time.

the sample cover, and the right side of the driver plate. This separation into parts is a result of poor polishing of the driver next to the sample well. The shock wave arrival at the driver plate free surface is indicated on one side by an apparent increase in reflectivity and on the other side by a decrease. The apparent increase is probably due to propellant gas that was shock-heated when the shock wave reached the free surface of the molybdenum driver plate. Note that some of the light and dark bands (due to scratches on the surface) can be followed across the shock wave arrival point and into the postshock region of the record. In some cases these bands are offset along the spatial axis by a slight shearing motion, and in other cases some bands dramatically change in intensity when the shock wave arrives. In cases in which the preshock and postshock light intensity is nearly equal, the changes in these bands are taken as reliable alternative indications of the shock arrival.

The shock wave arrival at the free surface of the cover is often more difficult to interpret than that of the driver because, as noted earlier, the shock wave intensity is lower in the cover than in the driver. In Figure 3, the shock wave appears to arrive much later at the center of the sample than at its perimeter as judged by the sharp cutoff in light intensity. Using the disturbances in light and dark bands to indicate the shock arrival, however, a more uniform shock wave arrival time is indicated. The variation in shock transit times across the cover indicated by the light and dark bands is commensurate with the calculated variation based on the measured curvature of the polished surfaces. Note that the shock wave is the first disturbance to reach the free surface: no elastic precursor waves have been detected in high-temperature Mo [*Miller et al.*, 1988]. Since the shock wave is the first disturbance to reach the free surface, we have in all cases interpreted the first disturbance measured on the streak record as the shock wave arrival; all subsequent features have been interpreted as postshock effects. Because the change in intensity of the light bands gives a variation in arrival time consistent with the measured surface curvature and because it occurs prior to any other change in the streak record in the sample region, we take this to be the true shock wave arrival time. A faint parabolic "shadow" can be seen in the region between the shock wave arrival and the cutoff of the reflected light. This parabolic shape is a characteristic postshock feature of high-temperature Mo [*Miller et al.*, 1988], consistent with our interpretation of this record. Although we chose to illustrate this particular record to show some of the complexities in interpretation, on other streak records the distinction between the shock wave arrival and the postshock image is as clear as the driver arrival shown in Figure 3.

3. ANALYTICAL PROCEDURE

The pressure-density state achieved in the shock experiment can be determined in an idealized experiment from measurement of the shock wave velocity in the sample and the particle velocity of the shocked sample. Neither of these measurements can be made directly in this experiment; both are indirectly determined. The sample shock wave velocity U_{ss} and sample particle velocity U_{ps} are determined by a coupled set of impedance-match equations for the flyer-driver, driver-sample, and sample-cover interfaces. The known impedance properties of the flyer plate and Mo container, together with the measured projectile velocity and shock wave propagation time, provide the necessary constraints for the impedance-match equations.

The streak camera record gives the transit time interval tt (Figure 3) for the shock wave to travel through the sample and the cap. The shock travels at a speed U_{sd} in the Mo driver plate, U_{ss} in the sample, and U_{sc} in the Mo cap:

$$tt = \frac{x_d}{U_{sd}} + \frac{x_s}{U_{ss}} + \frac{x_c}{U_{sc}}, \quad (1)$$

where the thickness of the sample at 1550°C is x_s, the thickness of the Mo cap is x_c, and the difference in thickness between the driver beneath the sample and the driver outside of the sample assembly is x_d. x_d is nominally zero; however, polishing and oxidation of the container make this dimension vary between +120 and -120 μm. x_d is positive when the driver plate extends into the sample well or negative if the sample well extends into the driver. These measurements are illustrated in the inset to Figure 1. The room temperature value of these thicknesses are determined from the sample container dimensions measured at various points in its preparation, and corrected for temperature with the thermal expansivity of Mo [*Touloukian et al.*, 1970]. Because of the driver plate and cover curvature, the thickness values used were those appropriate for the position on the streak record of the measured transit time. This set of measurements is therefore self-consistent, and different self-consistent sets give identical results within the propagated errors.

Flyer-Driver Impedance Match

The velocity of the flyer plate, in conjunction with its known shock impedance properties and those of the hot Mo [*Miller et al.*, 1988], suffice to determine the shock velocity in the driver, U_{sd}. The impedance match equation is a statement of stress equality at the flyer-driver interface:

$$P_d = \rho_{0d} U_{pd} (c_{0d} + s_d U_{pd})$$
$$= \rho_{0f} (V_{imp} - U_{pd}) \left[c_{0f} + s_f (V_{imp} - U_{pd}) \right], \quad (2)$$

where P_d is the shock pressure of the driver and V_{imp} is the projectile velocity. Equation (2) can be solved as a quadratic equation in U_{pd}.

The driver's shock velocity U_{sd} and particle velocity U_{pd} are related by an empirical constitutive equation:

$$U_{sd} = c_{0d} + s_d U_{pd}. \quad (3)$$

Equation (3) and an analogous constitutive equation for the flyer plate is implicit in (2). The parameters of the constitutive equations, and the initial densities of the driver (ρ_{0d}) and flyer (ρ_{0f}) are given in Table 2.

The shock density of the driver, ρ_d, is specified by its initial density and the shock and particle velocities by an equation of mass conservation across the moving shock front:

$$\rho_d = \rho_{0d} \frac{U_{sd}}{U_{sd} - U_{pd}}. \quad (4)$$

Driver-Sample Impedance Match

A similar impedance match can be made to determine the shock and particle velocities of the sample. The following equation is analogous to (2) and (3):

$$P_s = \rho_{0s} U_{ss} U_{ps}$$
$$\approx \rho_{0d} (2U_{pd} - U_{ps}) \left[c_{0d} + s_{0d} (2U_{pd} - U_{ps}) \right]. \quad (5)$$

The approximations used in this equation will be discussed below. Note that since a relationship between the sample shock velocity U_{ss} and the sample particle velocity U_{ps} is not yet known (this function is the objective of the experiments), (5) will serve as one of several coupled equations to be solved simultaneously for U_{ss} and U_{ps}.

The zero-pressure density of the 1550°C komatiite liquid, ρ_{0s} (given in Table 2), is not measured but calculated from the composition and temperature with the partial molar volume data of *Lange and Carmichael* [1987]. The shocked sample density at pressure P_s, ρ_s, is given by a mass balance equation analogous to (4):

$$\rho_s = \rho_{0s} \frac{U_{ss}}{U_{ss} - U_{ps}}. \quad (6)$$

Sample-Cover Impedance Match

The sample-cover impedance match equation is given by

$$P_c = \rho_{0c} U_{pc} (c_{0c} + s_s U_{pc})$$
$$\approx \rho_{0s} (2U_{ps} - U_{pc}) \left[c_{0s} + s_s (2U_{ps} - U_{pc}) \right]. \quad (7)$$

The approximations used in (7) are discussed below. A constitutive equation for the cover,

$$U_{sc} = c_{0c} + s_c U_{pc}, \quad (8)$$

is implicit in the impedance match (equation (7)). The shock density of the cover at shock pressure P_c is given by the mass balance equation:

$$\rho_c = \rho_{0c} \frac{U_{sc}}{U_{sc} - U_{pc}}. \quad (9)$$

TABLE 2. Material Properties

Parameter	Value	Unit	Reference
	Komatiite at 1550°C		
ρ_0	2.745±0.005	g/cm^3	1
α	$8.0\times10^{-5}\pm1.7\times10^{-5}$	K^{-1}	1
K_T	20.5±4.1	GPa	1
C_p	1.67±0.05	J/g K	2
$(\partial c_0/\partial T)_P$	$-1.4\times10^{-3}\pm0.9\times10^{-3}$	km/s K	3
η_s	4.3	P	4
	Mo at 1550°C		
ρ_0	9.924	g/cm^3	5
c_0	5.008	km/s	6
s	1.234	dimensionless	6
$L_{1550°C}/L_{20°C}$	1.0098±0.0005	dimensionless	7
	2024 *Al*		
ρ_0	2.785	g/cm^3	8
c_0	5.328	km/s	8
s	1.338	dimensionless	8
	Cu		
ρ_0	8.930	g/cm^3	8
c_0	3.940	km/s	8
s	1.489	dimensionless	8
	Ta		
ρ_0	16.654	g/cm^3	9
c_0	3.414	km/s	9
s	1.200	dimensionless	9
	W		
ρ_0	19.224	g/cm^3	9
c_0	4.029	km/s	9
s	1.237	dimensionless	9

References: 1, *Lange and Carmichael* [1987]; 2, *Stebbins et al.* [1984]; 3, *Rivers and Carmichael* [1987]; 4, *Bottinga and Weill* [1972]; 5, *Straumanis and Shodhan* [1968] and *Touloukian et al.* [1970]; 6, *Miller et al.* [1988]; 7, Linear thermal expansion ratio, *Touloukian et al.* [1970]; 8, *Marsh* [1980]; 9, *McQueen et al.* [1970].

In our experiments the driver and cap are both Mo and both initially at 1550°C; thus the numeric values of (ρ_{0d}, c_{0d}, s_d) are equal to (ρ_{0c}, c_{0c}, s_c). The shock states, however, are different ($U_{sd} \neq U_{sc}$, $U_{pd} \neq U_{pc}$, $\rho_d \neq \rho_c$, and $P_d \neq P_c$).

Full Solution

For each individual experiment, measurements (V_{imp}, x_d, x_s, x_c, and tt) are combined with the assumed shock parameters of the sample (c_{0s} and s_s, assuming a linear U_s–U_p relationship), the known impedance properties of the Mo driver/cap and flyer plate ($\rho_{0d/c}$, $c_{0d/c}$, $s_{0d/c}$, ρ_{0f}, c_{0f}, s_f), and the calculated value ρ_{0s}, to yield calculated values U_{ss} and U_{ps} for the sample. This solution is obtained from simultaneous solution of (1)-(9). For a series of experiments with different flyer plates and/or different impact velocities, a set of calculated U_{ss}-U_{ps} points is obtained. This set of values is then regressed to yield a new set of sample impedance parameters c_{0s} and s_s. The original data for each experiment are then reanalyzed with the new set of impedance parameters, etc., until convergence is achieved. The final converged values for c_{0s} and s_s are independent of the original assumed values.

The development presented above has presupposed that the experimental relationship between U_{ss} and U_{ps} will be linear. In practice, this assumption was not made. Rather, a set of equations analogous to those above was solved with a numeric method that allowed a variety of functional relationships ($U_{ss} = f(U_{ps})$) to be tried, e.g., quadratic and higher-order polynomial forms and piecewise linear functions. A linear relationship fit the data well, as is the usual case for crystalline and some amorphous materials over a range of shock stress.

With the assumption of normally distributed (Gaussian) errors, differential forms of (1)-(9) can be solved simultaneously to determine the uncertainty in U_{ss} and U_{ps} for each individual experiment. The error analysis (appendix) is done in conjunction with the determinations of U_{ss} and U_{ps}. The Hugoniot parameters c_{0s} and s_s are determined by a least squares procedure [*Bevington*, 1969] where each point is weighted by the inverse of its propagated error squared.

One additional assumption has been made in the preceding development. In a composite sample assembly, the impedance match solution for the flyer-driver interface uses the Hugoniot for two (initially) zero-pressure materials. All subsequent interfaces, however, involve impedance matching of a previously shocked material and an initially unshocked material. The impedance match equations for these interfaces require knowledge of the high-pressure impedance properties of the shocked material (i.e., the Hugoniot of the sample centered at the initial Hugoniot state). In our sample assembly we have two interfaces of this type: the driver-sample interface and the sample-cover interface.

At the driver-sample interface the driver plate will isentropically release to the sample shock pressure. This impedance match is rigorously given by a Riemann integral formulation:

$$\int_{U_{pd}}^{U_{ps}} dU_p = -\int_{P_d}^{P_s} dP \left[\rho_d K_{s,d}\right]^{-1/2}, \qquad (10)$$

where $K_{s,d}$ is the isentropic bulk modulus of the driver plate at high pressure. This integral expression can be approximated (to second order in U_{ps}) as

$$P_s = \rho_{0s} U_{ss} U_{ps}$$
$$= P_d + \rho_d (U_{pd} - U_{ps}) \left[c_d^{HP} + s_d^{HP}(U_{pd} - U_{ps})\right] \qquad (11)$$

by writing $K_{s,d}$ as $\rho_d (c_d^{HP})^2 + (4s_d^{HP} - 1)(P - P_d)$. The HP superscript denotes high-pressure values: c_d^{HP} and s_d^{HP} are the Hugoniot parameters of the driver centered at the high-pressure state P_d, and c_s^{HP} and s_s^{HP} are the Hugoniot parameters of the sample centered at P_s. This approximate solution of the exact Riemann integral resembles the Rankine-Hugoniot equation (e.g., equation (12)) because, to second order in U_p, the Hugoniot and isentrope are equivalent. At the sample-cover interface the shocked sample will be shocked again to the higher pressure of the shocked cover. Assuming a linear U_s-U_p relationship for the second shock of the sample, this impedance match is given by

$$P_c = \rho_{0c} U_{pc} (c_{0c} + s_c U_{pc})$$
$$= P_s + \rho_s (U_{ps} - U_{pc}) \left[c_s^{HP} + s_s^{HP}(U_{ps} - U_{pc})\right]. \qquad (12)$$

The high-pressure impedance properties of the shocked material (c^{HP} and s^{HP}) are not generally known, but they can be calculated from the standard impedance properties (c_0 and s) given knowledge of the thermodynamic Grüneisen parameter, $\gamma \equiv -\partial \ln T / \partial \ln V |_S$, and its isentropic volume derivative, $q \equiv \partial \ln \gamma / \partial \ln V |_S$:

$$(c^{HP})^2 = c_0^2 + 2c_0(2s-1)U_p + [1 - s(6 + \gamma - 5s)]U_p^2 + \frac{s}{c_0}[2 + \gamma + s(2s - \gamma - 4)]U_p^3, \qquad (13)$$

$$s^{HP} = \{16c_0^3 s + 8c_0^2 s(7s - 4 - \gamma)U_p + 4c_0 s[4(4s-1)(s-1) + \gamma(2q - \gamma - 5s)]U_p^2 + 12(s-1)s^2[2(s-1) - \gamma]U_p^3\} / \{16c_0[c_0^2 + c_0(3s-1)U_p + s(2(s-1) - \gamma)U_p^2]\}. \qquad (14)$$

A linear U_s-U_p relationship for the principal Hugoniot was assumed in deriving these expressions.

In the case of the driver-sample impedance match, (13) and (14) should be evaluated at P_d, the high-pressure state achieved by the flyer-driver impact. In practice, however, a simplifying assumption is often made for this impedance match. We imagine that a minuscule gap exists between the driver and the sample. If such a gap existed, then the driver would release to zero pressure prior to impact with the sample. If the release were isentropic, then the free surface of the driver would be traveling at twice the particle velocity. This impedance match thus resembles the flyer-driver impedance match where we substitute $2U_p$ for V_{imp}. The same assumptions were made for the sample-cover impedance match in (7). In instances where the free surface velocity is actually measured, this assumption has been found to be good [*Jeanloz and Ahrens*, 1979], and for solid-solid interfaces, the imaginary gap may in fact exist. In the solid-liquid case, however, the solid surface is wetted by the liquid and no such gap exists. Nevertheless, we tested the validity of this assumption by using the exact form of the impedance match (equation (11) for equation (5), and equation (12) for equation (7), with c^{HP} and s^{HP} evaluated with equations (13) and (14)). We assumed that the Grüneisen parameter varies with specific volume according to $d\gamma/dV = \gamma/V$ (q=1). Using these assumptions, we found that the results are similar whether the more precise equations or the gap approximations are used, so we used the fictitious gap assumption in all our data reduction.

The success of the fictitious gap assumption indicates that the impedance match equations are insensitive to γ; hence the more rigorous analysis cannot be used to constrain γ of molten komatiite in these experiments.

TABLE 3. Measured and Calculated Experimental Results

Shot	V_{imp}, km/s	Flyer	U_s, km/s	U_p, km/s	P, GPa	ρ, g/cm^3
754	1.127±0.007	2024 Al	3.85±0.05	0.47±0.01	5.0±0.1	3.13±0.01
785[a]	1.290±0.005	2024 Al	3.91±0.04	0.54±0.01	5.8±0.1	3.19±0.01
780	1.497±0.005	2024 Al	4.07±0.05	0.64±0.01	7.1±0.1	3.25±0.01
784[a]	1.767±0.007	2024 Al	4.26±0.05	0.76±0.01	8.8±0.1	3.34±0.01
782	1.912±0.007	2024 Al	4.31±0.05	0.82±0.01	9.7±0.1	3.39±0.02
777	1.420±0.005	Cu	4.61±0.06	1.02±0.02	12.8±0.2	3.52±0.02
755[a]	1.531±0.007	Cu	4.73±0.13	1.09±0.02	14.2±0.4	3.57±0.04
776	1.628±0.007	Cu	4.88±0.07	1.16±0.02	15.5±0.3	3.60±0.02
775	1.812±0.006	Cu	4.98±0.07	1.29±0.02	17.7±0.3	3.71±0.03
783[a]	1.694±0.007	W	5.47±0.09	1.60±0.02	24.0±0.4	3.88±0.04
781	1.872±0.006	W	5.76±0.10	1.75±0.02	27.7±0.5	3.94±0.04
753	2.496±0.009	Ta	6.21±0.05	2.10±0.02	35.7±0.4	4.15±0.03

[a] Vertical-slit streak record.

4. RESULTS

U_s–U_p Results

The results of 12 successful molten komatiite shock wave experiments are listed in Table 3 and shown in the U_s–U_p plane in Figure 4. The data clearly define a linear trend. A weighted least squares fit to the data (shown as a solid line in Figure 4) gives a U_s intercept c_0 of 3.13±0.03 km/s (1σ) and a slope s of 1.47±0.03 (1σ). No significant quadratic or higher-order terms are present. A linear U_s–U_p trend is observed for most materials [*Ruoff*, 1967; *Jeanloz and Grover*, 1988; *Jeanloz*, 1989], although several notable exceptions exist [e.g., *Rigden et al.*, 1988]. No theoretical justification for the linear function exists, but the absence of second- and higher-order terms implies the absence of fourth- and higher-order terms in the Eulerian finite strain EOS for typical values of the Grüneisen parameter [*Jeanloz and Grover*, 1988]. A linear U_s–U_p shock equation therefore often justifies the use of a third-order Birch-Murnaghan EOS to describe isentropic compression.

Each term in a Maclaurin series expansion of the general function $U_s = f(U_p)$ can be related to thermodynamic properties of the sample. Such relationships for the intercept, initial slope, and initial curvature are [*Ruoff*, 1967; *Jeanloz*, 1989]:

$$\lim_{U_p \to 0} U_s = c_0 = \sqrt{K_{0S} V_0}, \tag{15}$$

$$\lim_{U_p \to 0} \frac{dU_s}{dU_p} = s = \frac{1}{4}(K'_{0S} + 1), \tag{16}$$

$$\lim_{U_p \to 0} \frac{d^2 U_s}{dU_p^2} = 2s' = \frac{8K_{0S}K''_{0S} + (K'_{0S}+1)(7+4\gamma_0-K'_{0S})}{48c_0}, \tag{17}$$

where K_{0S} is the isentropic bulk modulus; K'_{0S} is the isentropic pressure derivative of K_{0S}; K''_{0S} is the isentropic pressure derivative of K'_{0S}; V_0 is the specific volume ($1/\rho_0$); c_0 is the bulk sound speed; and γ is the thermodynamic Grüneisen parameter. The zero subscripts denote evaluation at the preshock state; i.e., 0 bar and 1550°C in our experiments.

If we assume that the linear trend defined by our data from $U_p \approx 0.47$ to 2.10 km/s can be extrapolated to $U_p \to 0$, then the coefficients of our best fit line can be used with (15)-(17) to determine the isentropic bulk modulus of the molten komatiite

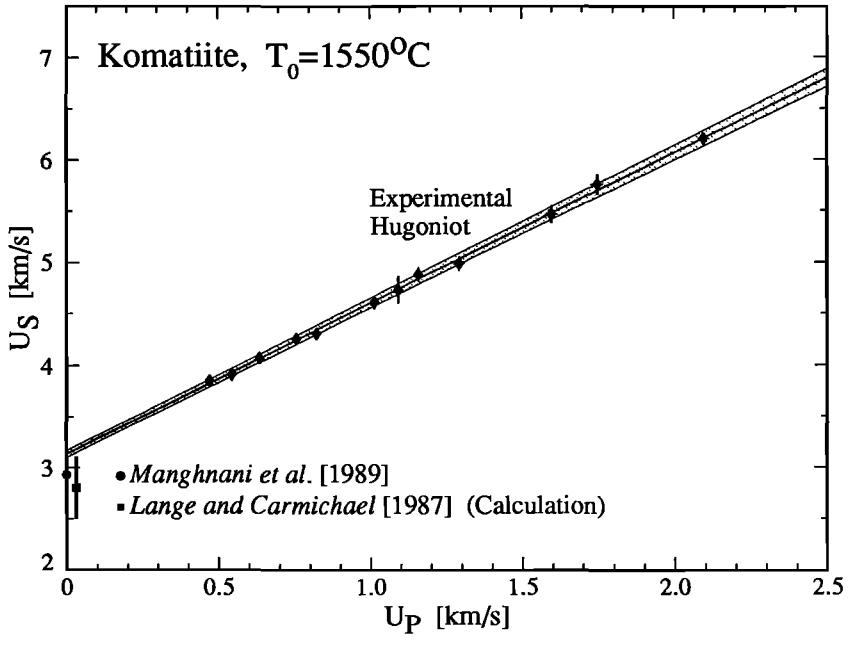

Fig. 4. Shock velocity U_s and particle velocity U_p data for 12 molten komatiite experiments. The ±1σ error bars lie within the symbols if not shown. The solid line is the weighted least squares best fit to the experimental data, U_s = 3.13 (±0.03) + 1.47 (±0.03) U_p (1σ errors). The shaded band represents the ±1σ error bound on the best fit line. The circle represents the measured ultrasonic sound speed of a 26.2 wt % komatiitic melt at 1558°C from *Manghnani et al.*, [1989] with a ±1σ error bar. The square represents the calculated bulk sound speed from the partial-molar properties of *Lange and Carmichael* [1987] with a ±1σ error bar, offset for clarity from its 1-bar pressure (U_p=0).

and its isentropic pressure derivatives. K_{0S} = 27.0 ± 0.6 GPa (1σ) from (15), and from (16) K'_{0S} = 4.9 ± 0.1 (1σ).

The absence of a quadratic term, s' (equation (17)), can be used to constrain K''_{0S} given an estimate of γ_0. The Grüneisen parameter can be calculated from the bulk modulus K_{0S}, specific volume V_0, heat capacity C_{P0}, and thermal expansivity α_0 with

$$\gamma_0 \equiv -\left.\frac{\partial \ln T}{\partial \ln V}\right|_S = \frac{\alpha_0 V_0 K_{0S}}{C_{P0}} = \frac{\alpha_0 V_0 K_{0T}}{C_{V0}}. \quad (18)$$

The heat capacity, 1.67 ± 0.05 J/g K [*Stebbins et al.*, 1984], and thermal expansivity, 8.0×10^{-5} ± 1.7×10^{-5} K^{-1} [*Lange and Carmichael*, 1987], are calculated from partial molar properties. With (18) the Grüneisen parameter is calculated to be 0.47 ± 0.10 (1σ) at 1550°C and 1 bar. With s' = 0, K''_{0S} = -0.109 ± 0.003 GPa^{-1} (1σ) (equation (17)), which differs from the -0.204 ± 0.014 (1σ) value implied by a third-order Birch-Murnaghan EOS ($K''_{0S} = [K'_{0S}(7-K'_{0S}) - 143/9]/K_{0S}$). If significant, this would imply that a fourth- or higher-order finite strain EOS is required. We note that if volume additivity is assumed for liquid constituents, then an nth-order finite-strain EOS for the end members implies an $(n+1)$th-order finite strain EOS for the ideal mixture. It would not be surprising, therefore, to discover higher-order terms in the equations of state of complex, multicomponent solutions.

The sound speed of a 26.2 wt % MgO komatiitic liquid was measured ultrasonically by *Manghnani et al.* [1989] to be 2.93 ± 0.15 km/s (1σ) at 1558°C (Figure 4). This value is close to our calculated 3.13 km/s, which lies within their ±2σ error bars. Nevertheless, the small difference may be significant. It is possible that the komatiitic liquid is more compressible at low pressure than our extrapolated shock data indicate. If we accept 2.93 km/s as the true 1 bar sound speed (i.e., c_0 = 2.93 km/s ± 0) and regress our data with this as a constraint, we find s = 1.63 ± 0.03 (1σ) and K'_{0S} = 7.5 ± 0.1 (1σ). Whether or not the difference between our extrapolated 1-bar sound speed and the ultrasonic measurements is real, we emphasize that the values of K_{0S} and K'_{0S} derived from our data are accurate parameters for characterizing the komatiite EOS in the pressure interval of our experiments.

The partial molar derivatives $\partial V_i/\partial P|_T$ from *Lange and Carmichael* [1987] can be used to compute the isothermal bulk modulus, K_{0T} = 20.5 ± 4.1 (1σ) GPa at 1550°C. The isentropic and isothermal bulk moduli are related by $K_{0S} = K_{0T}(1+\alpha_0\gamma_0 T_0)$, from which a bulk sound speed of 2.82 ± 0.3 (1σ) km/s is calculated. This calculated value is also shown in Figure 4. The partial molar calculated value is about 10% smaller than that inferred from the U_s–U_p fit (c_0 = 3.13 ± 0.03 km/s), but the latter lies within the 2σ bounds of the former. We consider this agreement to be good, especially considering the large uncertainties in α_0 and γ_0, and the fact that compositional extrapolation was required to apply the *Lange and Carmichael* [1987] coefficients.

A close correspondence between shock wave determinations of c_0 and ultrasonic measurements has also been observed for liquids in the system anorthite-diopside [*Rigden et al.*, 1984, 1988, 1989].

PV Systematics

The U_s–U_p data have been converted to the more familiar PV plane with equations (5) and (6). The PV data are shown in Figure 5 along with the calculated specific volume of our komatiite [*Lange and Carmichael*, 1987], and the best-fit U_s–U_p line (Figure 4), converted to a curve in the PV plane. The shock wave data span a pressure range from 5 to 36 GPa (50 to 360 kbar), and a compression range of 12-34%. In terms of depth within the Earth, this pressure range corresponds approximately to 150-950 km [*Dziewonski and Anderson*, 1981].

Rigden *et al.* [1989] proposed a semiquantitative model for the systematics of melt compression. They noted that oxides

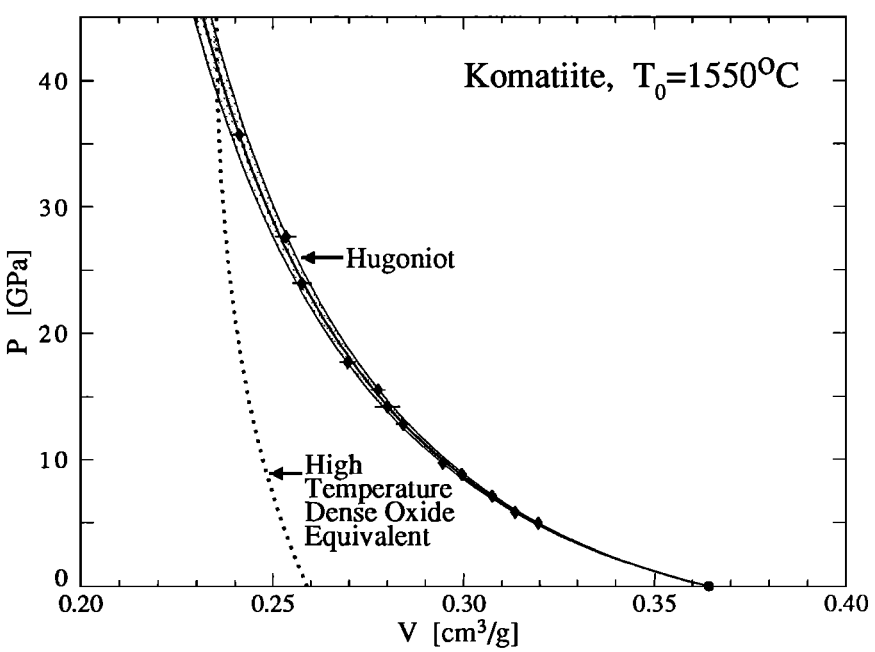

Fig. 5. Pressure-volume Hugoniot for molten komatiite. The ±1σ error bars lie within the symbol unless shown. The solid curve which passes through the experimental data is calculated from the best fit U_s–U_p line. The shaded band represents the ±1σ error bounds on this fit. The dotted curve is the calculated volume of a solid of komatiitic composition whose EOS is modeled as a mixture of high-pressure, high-temperature, dense oxides. The dense oxide volumes are calculated for the same pressure-temperature curve as the komatiite liquid Hugoniot.

like MgO and FeO have similar partial molar volumes in both low-pressure liquid and high-pressure crystalline phases, whereas the oxides SiO_2 and Al_2O_3 are much less dense in a low-pressure melt than in their high-pressure crystalline phases. This difference can be ascribed to the fact that in SiO_2 and Al_2O_3, Si^{4+} and Al^{3+} undergo gradual coordination number changes with O^{2-}, from IV to VI, with increasing pressure. Rigden et al. noted that, near 40 GPa, liquids in the system anorthite-diopside approach the densities of ideal mixtures of dense oxides to within 5-10%. Such a dense-oxide calculation was performed for the komatiite composition (Figure 5) using a simplified five-component model (SiO_2, MgO, FeO, Al_2O_3, and CaO, Table 4). The remaining components are not volumetrically significant, and therefore have little impact on the PV systematics. The dense-oxide PV curve has been adjusted to the calculated shock temperatures of the komatiite (discussed below) to facilitate direct comparison. At 40 GPa the specific volume of the crystalline dense oxide mixture is approximately equal to that of the komatiite, consistent with the prediction of their model. As remarked earlier, the incompressibility of the An-Di system increases rapidly with pressure when the density of the liquid approaches the density of the dense oxide mixture. By analogy, we might expect the komatiite to exhibit this stiffening behavior above ≈ 40 GPa (1000 km).

TABLE 4. EOS Parameters for Crystalline Oxides

	ρ_0, g/cm^3	K_{0S}, GPa	K'_{0S}	γ_0
Al_2O_3	3.988	252.7[a]	4.3[a]	1.32[a]
CaO	2.245	112.0[b]	4.8[b]	1.51[b]
FeO	5.864	158[c]	4[c]	1.63[b]
MgO	3.584	162.7[a]	4.27[a]	1.32[a]
SiO_2	4.290	316.0[d]	4[e]	1.25[e]

q is assumed to be 1.0, and C_V to be 3R/atom for all phases.
[a] *Anderson et al.* [1968].
[b] *Jeanloz and Ahrens* [1980].
[c] *Jeanloz and Sato-Sorensen* [1986].
[d] *Weidner et al.* [1982].
[e] *Lyzenga et al.* [1983].

Shock Temperatures

The shock wave EOS data specify the internal energy, pressure, and density of the high-pressure molten sample. However, the temperatures achieved in the shocked state have not been measured in these experiments and must be calculated. This temperature calculation relies heavily on the thermodynamic Grüneisen parameter, whose pressure and temperature dependence are poorly constrained. Shock wave experiments using porous samples suggest that γ is a weak function of specific volume. The functional form usually adopted for γ is

$$\gamma = \gamma_0\left[\frac{V}{V_0}\right]^q, \tag{19}$$

where [cf. *Bassett et al.*, 1968]

$$q \equiv \left.\frac{\partial \ln\gamma}{\partial \ln V}\right|_S = 1 + \gamma - K'_{0S} - \frac{1}{\alpha K_{0S}}\left.\frac{\partial K_S}{\partial T}\right|_P. \tag{20}$$

Using our shock wave data, values of γ_0 and α_0 discussed above, and using $\partial c_0/\partial T|_P = -1.4\times10^{-3} \pm 0.9\times10^{-3}$ km/s K [*Rivers and Carmichael*, 1987] to calculate the temperature derivative of K_{0S}, we calculate from (20) that $q = 8.8 \pm 7.9$ at 0 bar and 1550°C, the principal contribution to the uncertainty coming from α_0 [*Lange and Carmichael*, 1987]. Given the large error bars on q, we adopt the common assumption that $q=1$.

An interesting possibility arises in considering how to use q. Porous shock wave data suggests the form of (19). This form may be overly restrictive, however, particularly for liquids. Note that (19) prohibits γ from changing sign. If q were indeed large and if $\partial\gamma/\partial V$ were constant rather than $\partial\ln\gamma/\partial\ln V$, then γ could become negative at high pressure. Some liquids, most notably water, have negative γ in some PT interval. This could be very important for large magma bodies because a negative γ implies a negative α, which in turn means that a barrier to convection could exist.

Shock temperatures are calculated by numerical integration of the differential equation:

$$\left.\frac{\partial T}{\partial V}\right|_{Hugoniot} = \frac{2\gamma C_P T - V(P-P_0)(1+\alpha\gamma T) + K_S(V_0-V)}{C_P[\gamma(V_0-V) - 2V]}. \tag{21}$$

The formulation of *Walsh and Christian* [1955] is a special case of (21) for which $q=1$ and C_V is assumed constant. The remaining terms in (21) are evaluated at the appropriate high-pressure state. The high-pressure value of K_S is given by

$$K_S = \frac{U_s^2}{V_0(1-s\lambda)}\left[(1-\lambda)(1+s\lambda) - \gamma s\lambda^2\right], \tag{22}$$

where $\lambda = U_p/U_s$. A C_P or C_V function is required to calculate the temperature. From the 1-bar value of C_P, 1.67 ± 0.05 J/g K calculated from the partial molar properties given by *Stebbins et al.* [1984], we calculate $C_V = 1.56 \pm 0.06$ J/g K, and assume that C_V remains constant. The calculation of temperature then proceeds as follows: for each volume, γ is calculated from (19), then K_S is calculated from (22). With the constant value of C_V, α and C_P are calculated from (18) and $C_P = C_V(1+\alpha\gamma T)$. The derivative dT/dV is then evaluated (equation (21)) from these values of γ, α, K_S, C_P, and V. This derivative is used with the Bulirsch-Stoer numerical integration algorithm [*Press et al.*, 1988, pp. 582-588] to calculate T along the Hugoniot.

The deviation in P at constant V between the individual experiments and the best fit curve (Figure 5) are used to determine the deviation in T at constant V between the individual experiments and the curve obtained by integration of (21) with the equation

$$\left.\frac{\Delta T}{\Delta P}\right|_V \approx \left.\frac{\partial T}{\partial P}\right|_V = \frac{1}{\gamma\rho C_V}. \tag{23}$$

The calculated shock temperatures for the individual experiments and for the best fit line are shown in Figure 6 with their ±1σ errors. For comparison, the isentropic compression temperature, calculated directly from the definition of γ and (19), is also shown.

An estimate of the liquidus temperature of komatiite was constructed from available high-pressure melting experiments [*Bickle et al.*, 1977; *Takahashi and Scarfe*, 1985; *Scarfe and Takahashi*, 1986; *Wei et al.*, 1990]. According to our calculations the shocked komatiite is probably above its liquidus above 15 GPa and below 1 GPa, but in the 1-15 GPa range it is below its liquidus.

At ≈1-15 GPa our calculations suggest that the shock-compressed komatiite is in a field of crystal+liquid stability. Although some crystallization may have occurred below 15 GPa, the overall linearity of the U_s–U_p data is consistent with there being a single (metastable) liquid phase along the Hugoniot in this pressure range. However, it is possible that the change in specific volume associated with crystallization is too small to be detected within our ≈ 2% resolution [e.g., *Shaner*, 1981]. In some systems that undergo a phase change on the

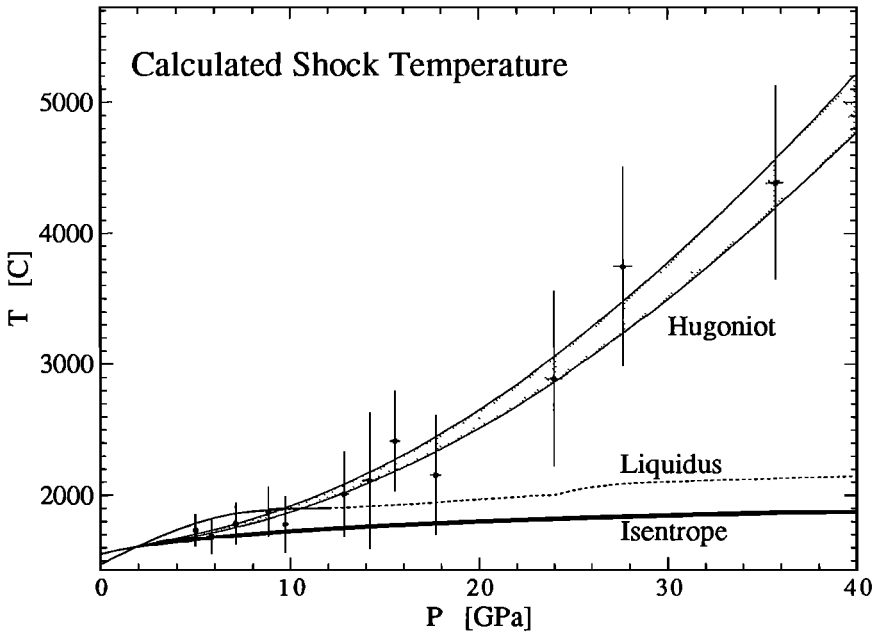

Fig. 6. Calculated shock and isentropic temperatures for molten komatiite.

Hugoniot, a two-wave shock structure may develop that is manifested in the U_s-U_p data as a discontinuous change in both slope and value. That we have not detected any such discontinuities in our results is consistent with, but does not prove, the idea that crystallization did not occur in our experiments.

We cannot rule out the possibility that crystallization occurred on the time scale of our experiments, but it seems unlikely. The good agreement shown in Figure 4 between our determination of K_{0S} and the experiments of *Manghnani et al.* [1989] and the calculated value from *Lange and Carmichael* [1987] supports the interpretation that the lower-pressure Hugoniot states are metastable liquid. Moreover, there is very little time available for crystallization in these experiments. The transit time of the shock wave across the komatiite sample is of the order of 900 ns (x_s/U_{ss}). We estimate the maximum degree of supercooling to be ≈ 120 K (Figure 6), giving an effective quench rate of 1.3×10^8 K/s. Although olivine, the liquidus phase in this region, is well known to crystallize rapidly from ultrabasic melts, it has been quenched with a splat quench technique [*Williams et al.*, 1989]. Splat quenching rates of 10^5 to 10^6 K/s were reported for the quenching of monticellite ($CaMgSiO_4$) composition [*McMillan*, 1984], and P. McMillan (personal communication, 1989) believes that the required quench rate for the formation of forsterite glass is similar to within an order of magnitude. If forsterite composition glasses can be quenched at rates of 10^7 K/s, then we consider it unlikely that olivine crystals could have formed during our experiments.

Bethe [1942] attributed a similar argument to J.G. Kirkwood. They suggested that explosions in water do not form ice VII, the equilibrium high-pressure phase, because the shock duration is shorter than the time scale for crystallization. In this case, the Hugoniot would follow the metastable extension of the liquid water curve.

State of Structural Relaxation

The objective of our experiments was to determine the equation of state of our molten komatiite under relaxed conditions. We used shock wave compression to achieve high-pressure states, and determined the pressure and density with the Rankine-Hugoniot relations. These relations are exact under either of two conditions [*Swan et al.*, 1973]: (1) they are applied across a discontinuous shock interface, or (2) they are applied across a continuous wave with a steady profile. If it can be demonstrated that the shock wave achieved a steady state profile during our experiments, then the Rankine-Hugoniot equations are applicable. As we discuss below, the steady wave condition also assures that the material properties determined from the Rankine-Hugoniot equations refer to a structurally relaxed state.

Bland [1965] investigated the shape of the shock front for viscous solids and determined that the shock profile becomes steady when the shock wave has propagated a distance of about 5 times its steady state thickness. The shock thickness is proportional to the viscosity and hence to the relaxation time of the sample [*Rivers and Carmichael*, 1987; *Kress et al.*, 1989]. The Rankine-Hugoniot equations will be applicable in a given experiment if the distance required for the shock to become steady is less than the sample thickness. *Swegle and Grady* [1985] defined the dimensionless Bland number, B, to be the ratio of the sample thickness to the distance which the wave must travel to reach steady state. If the Bland number is greater than 1 then the shock becomes stable before traversing the sample.

The Bland number can be approximated by [*Swegle and Grady*, 1985]

$$B = \frac{3s^2U_{ps}^2U_{ss}x_s}{16V_0c_0^2\eta_{eff}} \tag{24}$$

for a linear U_s-U_p material, where η_{eff} is an effective viscosity. If all relaxation mechanisms of the sample can be related to viscosity (e.g., by $\eta_s = \tau K_S$ where η_s is the shear viscosity, τ is the relaxation time, and K_S is the isentropic bulk modulus [*Rivers and Carmichael*, 1987]), then (24) will be a valid estimate of the Bland number. If there are relaxation mechanisms

with longer time scales than those associated with viscous flow, however, then (24) may be inadequate to evaluate the Bland criterion.

The effective viscosity in (24) is defined by dimensional arguments [*Jeanloz and Ahrens*, 1979] in terms of the shock front strain rate and deviatoric stress. Experimental measurements of the shock profile in water [*Harris and Presles*, 1981] suggest that this effective viscosity is similar to the shear viscosity. We estimate the effective viscosity of our komatiite to be equal to the 1-bar shear viscosity of 4.3 P (calculated from *Bottinga and Weill* [1972]). For an average sample thickness of 3.5 mm, we calculate Bland numbers of 720 at 5 GPa and 26,000 at 36 GPa. These numbers are >>1, suggesting that the shocks in our experiments successfully reached steady state. This, in turn, suggests that our experiments probe structurally relaxed, equilibrium states, since the shock can only be steady if the material behind the shock achieves a well-defined, unchanging state. If, however, komatiitic liquids have relaxation mechanisms whose time scales are $\geq 10^2$ times longer than the 16 ps relaxation time implied by the effective viscosity we have chosen, then the Bland criterion may not be satisfied at low shock pressure.

Although satisfaction of the Bland criterion assures the applicability of the Rankine-Hugoniot equations and the sampling of relaxed properties, the finite distance traveled by the shock before it reaches steady state contributes an inaccuracy into our determination of U_s. We experimentally determine the shock wave velocity by calculating the time necessary for the shock to traverse the sample thickness. If the Bland number is greater than 1 then the shock will travel a distance $x_s B^{-1}$ at some average velocity $U_{startup}$ while it is developing its steady profile, and a distance of $x_s(1-B^{-1})$ at its equilibrium velocity U_{eq}. We therefore measure a velocity,

$$U_{measured} \approx \frac{BU_{eq}}{B - 1 + \frac{U_{eq}}{U_{startup}}}, \quad (25)$$

that will differ from the desired value even though equilibrium is achieved in the experiment. We use c_0 as a conservative estimate of $U_{startup}$ to find the errors introduced in our measurement of U_s. From (25) and the Bland numbers calculated above we determine that our method of measurement introduced errors of 0.03% at 5 GPa and 0.002% at 36 GPa.

The Bland criterion [*Swegle and Grady*, 1985] differs from the criterion for reaching equilibrium in a shock experiment postulated by *Rigden et al.* [1988] and *Dingwell and Webb* [1989]. These authors suggest that the rise time of the shock front be compared to the relaxation time of the sample to determine whether or not equilibrium is achieved. They reasoned that when the rise time is shorter than the relaxation time, disequilibrium measurements may be made. However, the rise time of the shock is proportional to the viscosity [*Bland*, 1965; *Jeanloz and Ahrens*, 1979] which in turn is proportional to the relaxation time [*Rivers and Carmichael*, 1987; *Kress et al.*, 1989]. The rise of the shock front must be governed by the material's ability to respond to a stress gradient; thus the rise time should be of the same order as the relaxation time. Any gross discrepancies between calculated rise and relaxation times must be due to erroneous model assumptions. The rise time is only relevant in so far as it is related to the time needed for the shock to reach its steady state profile; that is, if the rise time exceeds the transit time of the shock through the sample, the Rankine-Hugoniot equations will clearly not apply and the experiments will be uninterpretable.

5. DISCUSSION

Comparison to Static Compression Experiments

Agee and Walker [1988] measured the compressibility of a komatiitic liquid near its liquidus by conducting sink/float bracketing experiments with olivine marker buoys. Liquid densities were bounded by the sink/float measurements and the calculated EOS of the olivine buoy. Experiments were not conducted on liquid komatiite directly but rather on komatiitic liquids into which varying amounts of fayalite had been dissolved; this was necessary to achieve olivine flotation in the 6 GPa range of their apparatus. Within their resolution, $\Delta\rho/\Delta P\ (P,T,X)$ was approximately constant, allowing linear extrapolation of their data to the liquid komatiite end member. Their end-member komatiite composition is essentially the same as our nominal komatiite composition.

We have calculated the EOS of our komatiite on its liquidus from our data using a Mie-Grüneisen thermal pressure correction. This calculation based on our data is compared with the *Agee and Walker* [1988] result in Figure 7. The high-pressure komatiite densities predicted by the static and dynamic experiments are identical, within errors, in the 0-6 GPa range of the static experiments. Note, however, that the slopes of the two equations of state, and hence K and K', are significantly different. Beyond ≈8 GPa the static and dynamic results diverge, with the static linear $P-\rho$ EOS predicting substantially higher densities.

Comparison to Liquidus Phases

The density of molten komatiite, calculated along its liquidus with the dynamic EOS and a Mie-Grüneisen thermal correction, is compared to the calculated high-pressure densities of phases on its liquidus (also at the komatiite liquidus temperature) in Figure 8. These mineral densities are calculated with a Mie-Grüneisen EOS:

$$P = P_S + P_T, \quad (26)$$

where P_S is the isentropic pressure calculated with a third-order isentropic Birch-Murnaghan EOS:

$$P_S = \frac{3}{2}K_{0S}\left[\left[\frac{\rho}{\rho_0}\right]^{7/3} - \left[\frac{\rho}{\rho_0}\right]^{5/3}\right]\times \left[1 - \frac{3}{4}(4-K'_{0S})\left[\left[\frac{\rho}{\rho_0}\right]^{2/3} - 1\right]\right], \quad (27)$$

and P_T is the thermal pressure at constant volume:

$$P_T = \gamma\rho C_V(T - T_S). \quad (28)$$

T_S is the isentropic temperature calculated from the definition of the Grüneisen parameter. Assuming $q=1$, equation (28) can be rewritten

$$P_T = \gamma_0\rho_0 C_V\left[T - T_0 e^{[\gamma_0(1-\rho_0/\rho)]}\right]. \quad (29)$$

Equation (26) is solved with a Newton-Raphson technique for density at each P-T point.

Olivine is the liquidus phase of ≈25 wt % MgO komatiite to approximately 5.6 GPa [*Bickle et al.*, 1977; *Wei et al.*, 1990]. Taking $K_D = (\mathrm{FeO/MgO})_{olivine}/(\mathrm{FeO/MgO})_{liquid}$ to be 0.30 + 0.02×P (P in GPa) [*Takahashi and Kushiro*, 1983] to 4 GPa, and 0.38 for higher pressures [*Agee and Walker*, 1988], the olivine in equilibrium with our komatiitic liquid changes from

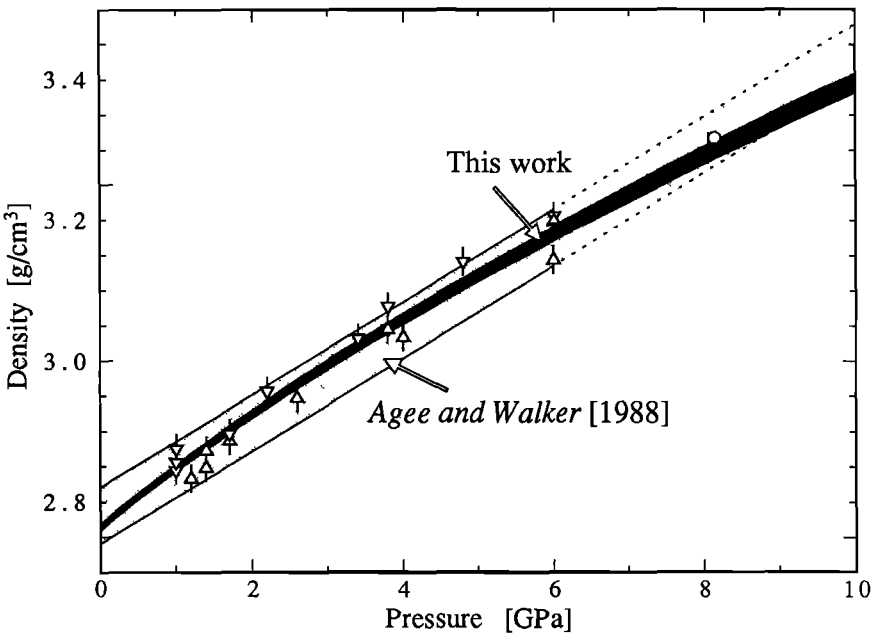

Fig. 7. A comparison of static and dynamic equations of state for komatiite on its liquidus. The static results of *Agee and Walker* [1988] are shown as downward pointing triangles for sinks ($\rho_{ol}>\rho_{liq}$) and upward pointing triangles for floats. The shaded band represents their quoted uncertainty. The open circle indicates the point at which they predict olivine (Fo_{94}) flotation on the komatiite liquidus. The solid band represents a calculation ($\pm 1\sigma$) based on our work and the estimated liquidus shown in Figure 6.

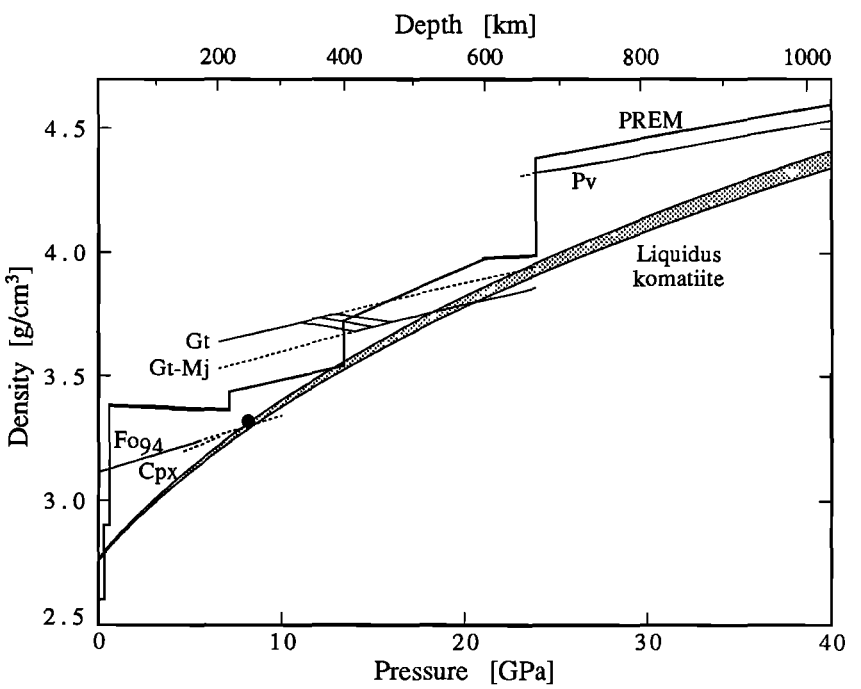

Fig. 8. The pressure-density relationships komatiite liquid ($\pm 1\sigma$) and its liquidus phases along the high-pressure liquidus. The liquidus temperature is shown in Figure 6. Liquidus phase relationships are taken from *Wei et al.* [1990], with the EOS parameters described in the text and given in Table 5 (Fo_{94}, olivine; Cpx, clinopyroxene; Gt, garnet; Gt–Mj, garnet-majorite; Pv, perovskite). Uncertainty in the garnet to garnet-majorite transition is indicated by the hatched region. Dashed lines indicate solid phase densities at liquidus temperatures, although the indicated phase is not in equilibrium with our komatiitic liquid under these conditions. Also shown is an estimate for the bulk mantle (PREM model [*Dziewonski and Anderson*, 1981]). The circle represents the point of olivine neutral density calculated by *Agee and Walker* [1988] at 8.1 GPa. Our data suggest that olivine would be neutrally buoyant near 8.2 GPa (252 km), although garnet is the liquidus phase at this pressure for a 25 wt % MgO komatiite.

Fo_{95} at 1 bar to Fo_{94} above 4 GPa. Since the equilibrium olivine composition is nearly constant, we adopt a single set of physical constants (Table 5).

At approximately 5.6 GPa a low-Ca clinopyroxene coexists with olivine and garnet near the liquidus of the ≈25 wt % MgO komatiite of Wei *et al.* [1990]. At 5.5 GPa and 1780°C *Wei et al.* [1990] report a near-liquidus Cpx of composition $Wo_{0.135}En_{0.742}Fs_{0.123}$ (molar). The EOS of this complex composition is calculated by adding volumes of appropriate quantities of diopside, bronzite ($En_{0.8}Fs_{0.2}$), and enstatite (Table 5).

Above 5.6 GPa the liquidus phase of ≈25 wt % MgO komatiite is a garnet [*Wei et al.*, 1990]. *Wei et al.* [1990] report a near-liquidus garnet composition of approximately $Py_{0.791}Alm_{0.110}Gr_{0.099}$ (molar) (Py, pyrope; Alm, almandite; Gr, grossularite) at 10 GPa and 1860°C, although their analyses indicate a small majorite component. The experiments of *Ohtani et al.* [1986] and *Irifune* [1987] indicate that the majorite content of garnets in equilibrium with peridotitic assemblages increases with pressure to 16 GPa but that near-liquidus garnets may have lower majorite contents. We spanned the range of probable liquidus garnet compositions by calculating both $Py_{0.791}Alm_{0.110}Gr_{0.099}$ and $Py_{0.316}Alm_{0.044}Gr_{0.040}Mj_{0.600}$ compositions. The EOS of these complex garnets are constructed from the end members (Table 5) with the assumption of volume additivity.

TABLE 5. EOS Parameters for Liquidus Phases

	ρ_0, g/cm^3	K_{0S}, GPa	K'_{0S}	γ_0
$Fo_{0.94}$	3.311[a]	129.4[a]	5.13[a]	1.15[a]
Di	3.276[b]	108[b]	4.8[b]	1.1[c]
$En_{0.8}Fs_{0.2}$	3.354[d]	103.5[d]	4.8[c]	1.1[c]
En	3.213[f]	107.8[g]	4.8[c]	1.1[c]
Py	3.562[h]	177[i]	4.5[i]	1.1[c]
Alm	4.318[j]	180.1[j]	4.59[j]	1.1[c]
Gr	3.617[k]	171.4[k]	4.25[k]	1.1[c]
Mj (En)	3.518[l]	160[m]	4.0[m]	1.1[c]
Pv ($En_{0.9}Fs_{0.1}$)	4.215[n]	262[o]	3.9[c]	1.7[n]

q is assumed to be 1.0, and C_V to be 3R/atom for all phases.
[a] *Kumazawa and Anderson* [1969].
[b] *Levien et al.* [1979*a*].
[c] *Watanabe* [1982].
[d] *Frisillo and Barsch* [1972].
[e] Value assumed.
[f] *Ohashi and Finger* [1976].
[g] *Weidner et al.* [1978].
[h] *Levien et al.* [1979*b*].
[i] *Leitner et al.* [1980].
[j] *Isaak and Graham* [1976].
[k] *Halleck* [1973].
[l] *Jeanloz* [1981].
[m] *Yagi et al.* [1987].
[n] *Jeanloz and Knittle* [1989].
[o] Isothermal value from reference *n* corrected to isentropic value.

Near 24 GPa both the olivine and pyroxene components of the mantle transform into the perovskite structure [*Liu*, 1979]. *Ito and Takahashi* [1987] found that a Mg-rich perovskite phase is the liquidus phase for a peridotitic composition near 25 GPa. Although high-pressure experiments on komatiitic compositions have not been carried out to these extreme pressures, we consider it likely that garnet-majorite will be replaced by perovskite as the first liquidus phase near 24 GPa.

The results presented in Figure 8 indicate that the komatiite composition used in this study is less dense than its assumed liquidus phases at all pressures to 40 GPa, except in the 20-24 GPa interval where majorite-rich garnet may be buoyant in coexisting komatiitic liquid. Thus, if this particular komatiite were formed in the upper mantle it would be buoyant relative to coexisting crystals and would tend to segregate upward. There is, however, substantial chemical variation in natural komatiites and related basalts, with MgO contents ranging from 10 to nearly 40 wt %. To a good first approximation, this variation is controlled by olivine addition or subtraction. As MgO content (and normative olivine) increases, olivine is stabilized on the komatiite liquidus to greater pressures. For example, experiments on a 31.5 wt % MgO komatiite [*Wei et al.*, 1990] show that such high MgO komatiites can have olivine as the liquidus phase to 9.6 GPa. Would olivine float in such a liquid at this pressure? The key to answering this question is understanding the effects of olivine addition and subtraction on melt density. This issue is addressed in the following section.

Compositional Variation

The compositional systematics of the EOS of multicomponent systems are of fundamental importance to the understanding of natural magmatic systems. As the melt fraction changes, due either to crystallization or melting, compositional changes will take place in the liquid unless the system is at an invariant point. For a ≈25 wt % MgO komatiite, olivine is the first liquidus phase to 5.6 GPa [*Wei et al.*, 1990], and crystallization of komatiite up to this pressure will result in a residual liquid that is more basaltic. A basaltic melt is less dense than a komatiitic melt at low pressure. At high pressure, however, basalt may be more dense than komatiite. This can be understood by considering the behavior of the major oxide components. The partial molar volume of MgO in a silicate melt at low pressure is similar to that of the high-pressure phase periclase, and we expect the compressibility of this component to be similar to that of the solid as well [*Rigden et al.*, 1989]. In contrast, although the partial molar volume of SiO_2 in a low pressure melt is substantially greater than that of stishovite, we expect this difference to diminish with increasing pressure. Moreover, although the "density" of the MgO component is greater than that of the SiO_2 component at low pressure, the reverse would be true at the high pressures where the partial molar volume of SiO_2 approaches the volume of solid stishovite. Thus, averaged over a several hundred kilobar pressure interval, siliceous liquids are expected to be more compressible than ultrabasic liquids, and as the partial molar volume of SiO_2 in the liquid approaches that of stishovite, the densities of more siliceous liquids will begin to overtake those of ultrabasic liquids. This qualitative trend is supported by shock wave data in the system anorthite-diopside [*Rigden et al.*, 1984, 1988, 1989], and when the densities of a liquid basalt analog in this system and liquid komatiite are compared at the same temperature, it can be shown that the analog basalt density is similar to the komatiite density near 25 GPa even though the komatiite is far denser at low pressure. Thus, although at lower pressures olivine fractionation leads to dramatic reduction in liquid density [*Sparks et al.*, 1980; *Stolper and Walker*, 1980], as pressure increases, the decrease in density with fractionation decreases, and there likely will be a pressure beyond which olivine fractionation would increase the liquid density.

If we adopt the liquid olivine EOS parameters proposed by *Rigden et al.* [1989], then we can calculate komatiite liquidus equations of state for a range of MgO contents by assuming ideal mixing with respect to volume of olivine liquid and komatiite liquid. This calculation is presented in Figure 9 for MgO contents ranging from 6.9 to 35.3 wt %. We have approximated the effect of adding (and subtracting) olivine on the liquidus

temperature by adding (or subtracting) 20°C per wt % MgO relative to our nominal composition [*Nisbet*, 1982]. Although this approximation is probably good at near crustal pressures, the experimental data of Wei *et al.* [1990] (for 25 and 31.5 wt % MgO komatiites) indicates that the MgO dependence of the liquidus may be much smaller at high pressure. A more precise calculation of the fusion curves [*Walker et al.*, 1988] is underconstrained by the available data but would likely have little effect on the resulting calculations because α is so small. This diagram illustrates three important points: First, near 13.3 GPa the assimilation or fractionation of olivine will not significantly change the density of the melt; that is, basaltic through peridotitic magmas will have nearly the same density at their 13.3 GPa liquidi. At greater pressure the density of basaltic liquids exceeds that of the peridotitic liquids. This result was anticipated by the calculations of *Ohtani* [1984] and *Rigden et al.* [1989]. Second, if we use the olivine±clinopyroxene±garnet cosaturation point to indicate the probable origin of these

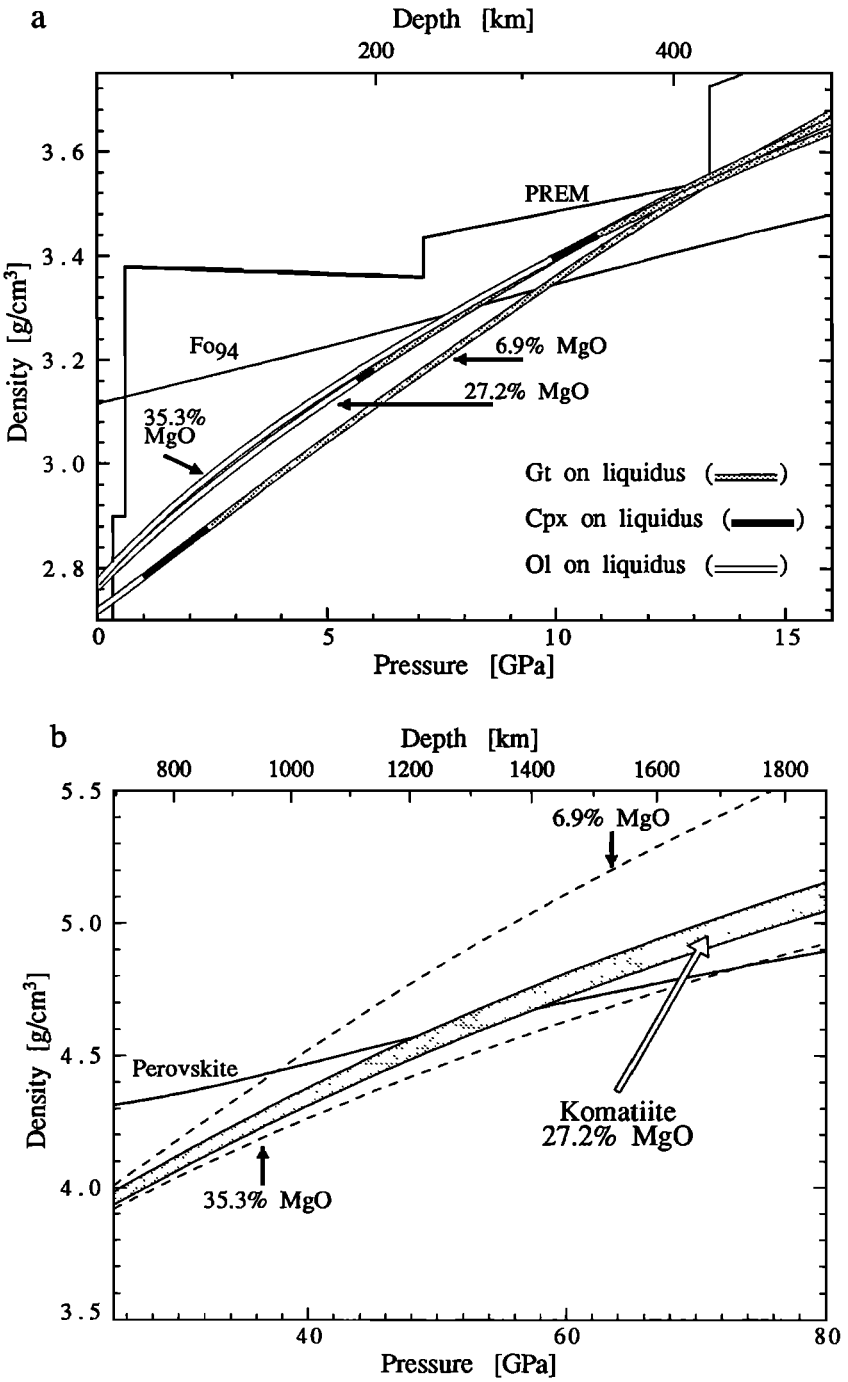

Fig. 9. Komatiitic liquid liquidus equations of state calculated from our experimental data and the proposed liquid olivine EOS of *Rigden et al.* [1989]. Curves are komatiite with 50 wt % subtracted olivine (6.9% MgO), komatiite (27.2% MgO), and komatiite with 50% added olivine (35.3% MgO). The liquid Fo/Fa component contents of the various liquids were determined by assuming Rayleigh fractionation with K_D=0.38. Liquidus temperatures were adjusted from Figure 6 according to the MgO content by adding 20°C per wt % added MgO [*Nisbet*, 1982]. The curves are open where olivine is estimated to be the liquidus phase, bold where clinopyroxene is estimated to be the liquidus phase, and shaded where garnet is estimated to be the liquidus phase. The equation of state of crystalline olivine is the same as in Figure 7. (*a*) Calculation in the pressure range of our experiments. (*b*) Extrapolated to lower mantle conditions.

ultramafic magmas, then komatiites with MgO >30 wt % will originate under conditions where both olivine and clinopyroxene would float. Third, it is interesting to note that at the 13.3 GPa point where all komatiitic magmas have similar density, their density is approximately equal to that of the bulk mantle (PREM model [*Dziewonski and Anderson*, 1981]).

If substantiated by further experiments, the coincidence of all basaltic through peridotitic liquidus equations of state both with each other and with the bulk mantle would imply that it would be difficult for such magmas to ascend from below 400 km. Although komatiitic liquids would be capable of separating (up) from their coexisting crystals, the negligible density contrast between the liquid and bulk mantle at this point might inhibit separation of the liquid from its bulk mantle environment. Figure 9 indicates that the spectrum of magma compositions from basaltic through peridotitic are approximately equal in density to the bulk cold mantle as represented by the PREM model. If we allow for either a hotter Archaean geotherm or a thermal aureole surrounding the anomalously hot magma body, then the bulk mantle density near the magma body would likely be lower than the cold PREM estimate. Moreover, increasing temperature shifts the olivine $\rightarrow \beta$ transition to higher pressures by 0.0025 GPa/°C [*Katsura and Ito*, 1989] thereby enlarging the region in which komatiites are negatively buoyant in the bulk mantle by moving the 400-km discontinuity to greater depth. The small positive temperature dependence for the reaction En→Mj (0.0015 GPa/°C [*Irifune*, 1987)] has less effect on the high-temperature density profile of the transition zone.

In Figure 9*b* we show this same calculation for lower mantle conditions. The results must be considered speculative since our data have been extrapolated well beyond the 36 GPa limit of our experiments. This calculation indicates that perovskite, ostensibly the densest lower mantle crystalline phase, may be less dense than the range of basic to ultrabasic magma compositions. If this is true, then ultrabasic magmas would be incapable of ascending from below ≈1000 km. *Ohtani* [1983] arrived at the same conclusion and suggested that downward migration of melts in the lower mantle would transport incompatible and radiogenic elements toward the core. We note that although intriguing, this suggestion is uncertain since there are circumstances under which sinking magmas would freeze on adiabatic descent or on downward flow through a porous mush even if denser than their coexisting mineral phases.

While neutral or negative buoyancy would preclude the upward segregation of a liquid from a static matrix, it might be possible to extract the liquid if the matrix were transported upward in part of a large-scale convection system. In this case, both liquid and solid would rise together until the density contrast becomes sufficient for separation to occur. Thus when partial melting is initiated by the adiabatic decompression of upwelling mantle plumes, continued upward transport of the plume may permit escape of the liquid even if it were initially too dense to do so. This may lead to magmas produced by relatively large degrees of partial melting by a process approaching equilibrium, batch melting; magmas of this sort may be difficult to generate if melting begins at conditions of lower pressure at which the melt is always less dense than coexisting crystals and drains quickly upward, away from residual crystals [*Stolper et al.*, 1981; *McKenzie*, 1984].

6. CONCLUSIONS

We have measured the Hugoniot of a molten komatiite initially at 1550°C. The data are smooth, indicating that discontinuous changes in melt structure (or changes occurring over narrow pressure intervals) have either not occurred or are too subtle to be detected in the 5-36 GPa range of our experiments. This result is consistent with Hugoniot measurements on molten diopside and anorthite [*Rigden et al.*, 1989] but differs from molten $An_{0.64}Di_{0.36}$ eutectic composition Hugoniot results [*Rigden et al.*, 1988] and possibly molten perovskite diamond cell results [*Knittle and Jeanloz*, 1989] that may suggest such liquid-state structural changes. The isentropic bulk modulus is determined to be 27.0 ± 0.6 (1σ) GPa, and its isentropic pressure derivative is 4.9±0.1 (1σ). The pressure-density relationship obtained from these parameters is consistent with the static compression measurements of *Agee and Walker* [1988] to 6 GPa but differs at higher pressure.

The 1550°C Hugoniot may lie below the komatiite liquidus at pressures less than 15 GPa. Our data show no evidence of crystallization or vitrification. The kinetics of olivine crystallization support the idea that our samples remained molten, albeit metastably, below 15 GPa. To the extent that shear viscosity is a valid indication of the relaxation time, we believe the shock states achieved represent fully relaxed liquids.

We confirm the hypothesis that ultrabasic liquids can be more dense than coexisting crystals at upper mantle pressures [*Stolper et al.*, 1981; *Ohtani*, 1983, 1984]. Olivine and clinopyroxene are neutrally buoyant between 7 and 9 GPa, depending on the specific liquid composition. Garnet-majorite may be buoyant in ultrabasic compositions in the 20-24 GPa interval. Extrapolating our data to 70 GPa, we suggest that perovskite could be buoyant in ultrabasic liquids in the lower mantle. Under upper mantle conditions, increasing the normative olivine content of a liquid increases its density. We predict, however, that at pressures above 13.3 GPa, increasing the normative olivine content of basic and ultrabasic liquids will decrease the liquid density.

APPENDIX

The analysis of an individual molten silicate shock experiment requires that a set of nine algebraic formulae (equations (1)-(9)) be solved simultaneously. This solution is only approximate, however, since results from a series of experiments are needed to find the c_{0s} and s_s parameters required for the sample-cover impedance match. A complete reduction of the experimental data for a series of N individual experiments therefore requires the simultaneous solution of 9N+2 equations: equations (1)-(9) for each experiment, and two regression equations to determine c_{0s} and s_s. Rather than solving 110 simultaneous equations for 12 experiments, we used an iterative approach. Beginning with assumed values for c_{0s} and s_s, we could analyze each experiment with nine equations. The second step of this iterative procedure was to calculate new updated values of c_{0s} and s_s.

This iterative approach cannot be used in the calculation of propagated errors. If we computed errors in U_{ss} and U_{ps} including error contributions from c_{0s} and s_s, and then used these quantities in a weighted least squares fit to recalculate both c_{0s} and s_s and their formal errors, then the errors would increase without bound with successive iterations. To properly calculate the propagated errors, a minimum of 6N+2 (six equations per experiment, discussed below, and two equations for c_{0s} and s_s) linear equations must be solved simultaneously to determine the uncertainties in c_0 and s together with N uncertainties in U_{ss}, U_{ps}, P_s, and ρ_s. Although this approach would be rigorous, it is not particularly instructive because the relative importance of various measurements cannot readily be deter-

mined. Because the contributions of c_{0s} and s_s to the uncertainty in each individual experiment are small, we can decouple the 6N+2 simultaneous equations into N sets of six simultaneous equations, six equations per experiment.

In the following error analysis we will consider the contribution of the error in our measurements, and in the uncertainty in the calculated value ρ_{0s}, to the error in U_{ss}, U_{ps}, P_s, and ρ_s. Individual experiments will be analyzed separately by ignoring the contribution of c_{0s} and s_s.

The minimum six equations which must be solved simultaneously to determine U_{ss}, U_{ps}, P_s, and ρ_s are (1) the flyer-driver impedance match (second equality of equation (2)), (2) the driver-sample impedance match (second equality of equation (5)), (3) the sample-cover impedance match (second equality of equation (7)), (4) the equation for the total shock wave transit time (equation (1) with equations (3) and (8)),

$$tt = \frac{x_s}{U_{ss}} + \frac{x_d}{c_{0d} + s_d U_{pd}} + \frac{x_c}{c_{0c} + s_c U_{pc}}, \qquad \text{(A1)}$$

(5) the sample stress balance equation (first equality of equation (5)), and (6) the equation of mass conservation for the sample (equation (6)).

In these equations, the dependent variables are U_{pd}, U_{pc}, U_{ps}, U_{ss}, P_s, and ρ_s. We will consider V_{imp}, tt, x_d, x_s, x_c, and ρ_{0s} to be independent variables that contribute error to the determination of the dependent variables. The remaining parameters are considered as exact constants.

The sensitivity of the dependent variables to changes in the independent variables is determined by the partial derivative. Because these equations are coupled, however, the partial derivatives cannot be immediately determined. The differential forms the six basic equations are linear, however, and can be decoupled with a simple matrix equation:

$$\begin{bmatrix} d U_{ss} \\ d U_{ps} \\ d P_s \\ d \rho_s \\ d U_{pd} \\ d U_{pc} \end{bmatrix} = \mathbf{E} \times \begin{bmatrix} d V_{imp} \\ d tt \\ d x_d \\ d x_s \\ d x_c \\ d \rho_{0s} \end{bmatrix}, \qquad \text{(A2)}$$

where E is a 6×6 matrix of partial derivatives. The matrix E is given by

$$\begin{bmatrix} 0 & 0 & 0 & 0 & \cdots \\ \rho_{0s} U_{ps} & \rho_{0s} U_{ss} + \rho_{0d}(c_{0d} + 2 s_d (2U_{pd} - U_{ps})) & 0 & 0 & \cdots \\ 0 & -2\rho_{0s}(c_{0s} + 2 s_s (2U_{ps} - U_{pc})) & 0 & 0 & \cdots \\ \dfrac{x_s}{U_{ss}^2} & 0 & 0 & 0 & \cdots \\ -\rho_{0s} U_{ps} & -\rho_{0s} U_{ss} & 1 & 0 & \cdots \\ \dfrac{\rho_{0s} U_{ps}}{(U_{ss} - U_{ps})^2} & \dfrac{\rho_{0s} U_{ss}}{(U_{ss} - U_{ps})^2} & 0 & 1 & \cdots \end{bmatrix}$$

$$\times \begin{bmatrix} \left\{ \begin{matrix} \rho_{0d}(c_{0d} + 2 s_d U_{pd}) + \\ \rho_{0f}(c_{0f} + 2 s_f (V_{imp} - U_{pd})) \end{matrix} \right\} & 0 \\ -2\rho_{0d}(c_{0d} + 2 s_d (2U_{pd} - U_{ps})) & 0 \\ 0 & \left\{ \begin{matrix} \rho_{0c}(c_{0c} + 2 s_c U_{pc}) + \\ \rho_{0s}(c_{0s} + 2 s_s (2U_{ps} - U_{pc})) \end{matrix} \right\} \\ \dfrac{s_d x_d}{U_{sd}^2} & \dfrac{s_c x_c}{U_{sc}^2} \\ 0 & 0 \\ 0 & 0 \end{bmatrix}^{-1}$$

$$\times \begin{bmatrix} \rho_{0f}(c_{0f} + 2 s_f (V_{imp} - U_{pd})) & 0 & 0 & 0 & 0 & 0 \\ 0 & 0 & 0 & 0 & 0 & \dfrac{-P_s}{\rho_{0s}} \\ 0 & 0 & 0 & 0 & 0 & \dfrac{P_c}{\rho_{0s}} \\ 0 & -1 & \dfrac{1}{U_{ss}} & \dfrac{1}{U_{sd}} & \dfrac{1}{U_{sc}} & 0 \\ 0 & 0 & 0 & 0 & 0 & \dfrac{P_s}{\rho_{0s}} \\ 0 & 0 & 0 & 0 & 0 & \dfrac{\rho_s}{\rho_{0s}} \end{bmatrix} \equiv \mathbf{E}. \qquad \text{(A3)}$$

The rows of E correspond to the differential forms the six equations in the order given above. The partial derivative of any dependent variable with respect to any independent variable can be found from the appropriate element of the matrix E. If errors are assumed to be normally distributed (Gaussian), then the variance in a dependent variable, X_i, is related to the variance of the independent variables, χ_j, according to

$$\sigma_{X_i}^2 = \sum_j \left[\frac{\partial X_i}{\partial \chi_j} \right]^2 \sigma_{\chi_j}^2 = \sum_j \left[\mathbf{E}_{i,j} \right]^2 \sigma_{\chi_j}^2. \qquad \text{(A4)}$$

If we form a new matrix $\mathbf{E}^2$ such that $\mathbf{E}^2_{i,j} = (\mathbf{E}_{i,j})^2$, then the variances in the dependent variables can be readily calculated from

$$\begin{bmatrix} \sigma_{U_{ss}}^2 \\ \sigma_{U_{ps}}^2 \\ \sigma_{P_s}^2 \\ \sigma_{\rho_s}^2 \\ \sigma_{U_{pd}}^2 \\ \sigma_{U_{pc}}^2 \end{bmatrix} = \mathbf{E}^2 \times \begin{bmatrix} \sigma_{V_{imp}}^2 \\ \sigma_{tt}^2 \\ \sigma_{x_d}^2 \\ \sigma_{x_s}^2 \\ \sigma_{x_c}^2 \\ \sigma_{\rho_{0s}}^2 \end{bmatrix}. \qquad \text{(A5)}$$

The relative magnitude of the $\mathbf{E}^2$ matrix elements shows their relative importance in the experiments. This matrix is presented for shot 755, which is near the median of the shock pressure range of our experiments:

$$\begin{bmatrix} \sigma_{U_{ss}}^2 \\ \sigma_{U_{ps}}^2 \\ \sigma_{P_s}^2 \\ \sigma_{\rho_s}^2 \\ \sigma_{U_{pd}}^2 \\ \sigma_{U_{pc}}^2 \end{bmatrix} = \begin{bmatrix} 1.10\times10^{-2} & 48.3 & 1.34 & 1.94 & 1.46 & 8.88\times10^{-4} \\ 0.586 & 0.119 & 3.31\times10^{-3} & 4.81\times10^{-3} & 3.61\times10^{-3} & 7.88\times10^{-3} \\ 102. & 399. & 11.0 & 16.1 & 12.1 & 26.3 \\ 0.636 & 4.68 & 0.130 & 0.189 & 0.141 & 1.61 \\ 0.221 & 0. & 0. & 0. & 0. & 0. \\ 0.105 & 7.33\times10^{-3} & 2.03\times10^{-4} & 2.95\times10^{-4} & 2.21\times10^{-4} & 7.14\times10^{-3} \end{bmatrix} \times \begin{bmatrix} \sigma_{V_{imp}}^2 \\ \sigma_{tt}^2 \\ \sigma_{x_d}^2 \\ \sigma_{x_s}^2 \\ \sigma_{x_c}^2 \\ \sigma_{\rho_{0s}}^2 \end{bmatrix}. \qquad \text{(A6)}$$

where all velocities are in units of km/s or mm/μs, time is measured in μs, distances in mm, and densities in g/cm^3.

This equation was used in the evaluation of errors for shot 755, and analogous equations (calculated from equation (A3)) were used for the other experiments. These errors are reported in Table 3.

To illuminate the relative importance of the various error terms, it is necessary to scale (A6). Defining $\varepsilon_{X_i} \equiv \sigma_{X_i}/X_i$, a scaled uncertainty, (A6) can be rewritten

$$\begin{bmatrix} \varepsilon^2_{U_{ss}} \\ \varepsilon^2_{U_{ps}} \\ \varepsilon^2_{P_s} \\ \varepsilon^2_{\rho_s} \\ \varepsilon^2_{U_{pd}} \\ \varepsilon^2_{U_{pc}} \end{bmatrix} = \begin{bmatrix} 2.30\times10^{-5} & 1.33 & 8.12\times10^{-4} & 0.995 & 3.39\times10^{-2} & 6.80\times10^{-5} \\ 1.13 & 4.68\times10^{-2} & 2.86\times10^{-5} & 3.50\times10^{-2} & 1.19\times10^{-3} & 3.46\times10^{-2} \\ 1.10 & 0.878 & 5.36\times10^{-4} & 0.657 & 2.24\times10^{-2} & 0.649 \\ 0.105 & 0.169 & 1.04\times10^{-4} & 0.127 & 4.32\times10^{-3} & 0.896 \\ 1.10 & 0. & 0. & 0. & 0. & 0. \\ 0.959 & 2.08\times10^{-2} & 1.27\times10^{-5} & 1.56\times10^{-2} & 5.32\times10^{-4} & 0.172 \end{bmatrix} \times \begin{bmatrix} \varepsilon^2_{V_{imp}} \\ \varepsilon^2_{tt} \\ \varepsilon^2_{x_d} \\ \varepsilon^2_{x_s} \\ \varepsilon^2_{x_c} \\ \varepsilon^2_{\rho_{0s}} \end{bmatrix}. \quad \text{(A7)}$$

A 10% error in the transit time, tt, therefore contributes 4% error to ρ_s ($\sqrt{0.169\times(0.10)^2}=0.04$) and contributes nothing to the error in U_{pd} as expected. The relative importance of the measured values is different for each dependent variable. The transit time is the most important term for U_{ss} and the second most important for U_{ps}. The flyer plate velocity is the most important term for U_{ps}, but this term is unimportant for U_{ss}. Neither U_{ps} nor U_{ss} rely heavily on ρ_{0s}; thus the bulk sound speed and K'_{0S} are not strongly dependent on the initial density calculation. The bulk modulus, $K_{0S}=\rho_{0S}c^2_{0s}$, however, is strongly dependent on this calculated value.

Acknowledgements. We thank G. Fine at Corning Technical Center, Corning, New York, for the komatiite starting materials. M. Long, E. Gelle, and A. Campbell (University of Chicago) provided expert assistance in the preparation and execution of the shock experiments. We appreciate the use of the rf heater provided by L.T. Silver. We are grateful to D.J. Stevenson, D.L. Anderson, and N.T. Arndt (Max-Planck-Institut für Chemie, Mainz) for their thoughtful comments and suggestions and K. Wei and R.G. Tronnes (University of Alberta) for sharing their unpublished manuscript with us. This manuscript has benefited greatly from careful review by D. Walker. This work was funded by the National Science Foundation grants EAR-86-18545 and EAR-89-16753. Contribution 4809, Division of Geological and Planetary Sciences, California Institute of Technology, Pasadena, California.

REFERENCES

Abe, Y., and T. Matsui, Early evolution of the Earth: Accretion, atmosphere formation, and thermal history, *Proc. Lunar Planet. Sci. Conf. 17th*, part 1, *J. Geophys. Res., 91*, suppl., E291-E302, 1986.

Agee, C.B., and D. Walker, Olivine flotation in a chondritic mantle (abstract), *Meteoritics, 22*, 314, 1987.

Agee, C.B., and D. Walker, Static compression and olivine flotation in ultrabasic silicate liquid, *J. Geophys. Res., 93*, 3437-3449, 1988.

Ahrens, T.J., Earth accretion, in *Origin of the Earth*, edited by H.E. Newsom and J.H. Jones, pp. 211-227, Oxford University Press, New York, 1990.

Ahrens, T.J., J.H. Lower, and P.L. Lagus, Equation of state of forsterite, *J. Geophys. Res., 76*, 514-528, 1971.

Anderson, O.L., R.C. Schreiber, R.C. Liebermann, and N. Soga, Some elastic constant data on minerals relevant to geophysics, *Rev. Geophys., 6*, 491-524, 1968.

Bassett, W.A., T. Takahashi, H.-K. Mao, and J.S. Weaver, Pressure-induced phase transformation in NaCl, *J. Appl. Phys., 39*, 319-325, 1968.

Benz, W., W.L. Slattery, and A.G.W. Cameron, The origin of the Moon and the single-impact hypothesis I, *Icarus, 66*, 515-535, 1986.

Benz, W., W.L. Slattery, and A.G.W. Cameron, The origin of the Moon and the single-impact hypothesis, II, *Icarus, 71*, 30-45, 1987.

Bethe, H.A., The theory of shock waves for an arbitrary equation of state, *Office of Scientific Research and Development*, 545, 84 pp., 1942.

Bevington, P.R., *Data Reduction and Error Analysis for the Physical Sciences*, pp. 92-118, McGraw-Hill, New York, 1969.

Bickle, M.J., C.E. Ford, and E.G. Nisbet, The petrogenesis of peridotitic komatiites: Evidence from high-pressure melting experiments, *Earth Planet. Sci. Lett., 37*, 97-106, 1977.

Bland, D.R., On shock structure in a solid, *J. Inst. Math Appl., 1*, 56-75, 1965.

Bottinga, Y., and D.F. Weill, The viscosity of magmatic silicate liquids: A model for calculation, *Am. J. Sci., 272*, 438-475, 1972.

Cameron, A.G.W, and W. Benz, Possible scenarios resulting from the giant impact (abstract), *Lunar Planet. Sci. Conf., 20*, 137-138, 1989.

Dingwell, D.B., and S.L. Webb, Structural relaxation in silicate melts and non-Newtonian melt rheology in geologic processes, *Phys. Chem. Miner., 16*, 508-516, 1989.

Dziewonski, A.M., and D.L. Anderson, Preliminary reference Earth model, *Phys. Earth Planet. Iner., 25*, 297-356, 1981.

Frisillo, A.L., and G.R. Barsch, Measurement of single-crystal elastic constants of bronzite as a function of pressure and temperature, *J. Geophys. Res., 77*, 6360-6384, 1972.

Green, D.H., and A.E. Ringwood, The genesis of basaltic magmas, *Contrib. Mineral. Petrol., 15*, 103-190, 1967.

Halleck, P.M., The compression and compressibility of grossular garnet: A comparison of X-ray and ultrasonic methods, Ph.D. thesis, pp. 82, Univ. of Chicago, Ill., 1973.

Harris, P., and H.N. Presles, Reflectivity of a 5.8 kbar shock front in water, *J. Chem. Phys., 74*, 6864-6866, 1981.

Herzberg, C.T., Magma density at high pressure, part 1, The effect of composition on the elastic properties of silicate liquids, in *Magmatic Processes: Physiochemical Principles*, edited by B.O. Mysen, pp. 25-46, Geochemical Society, Washington, D.C., 1987.

Irifune, T., An experimental investigation of the pyroxene-garnet transformation in a pyrolite composition and its bearing on the constitution of the mantle, *Phys. Earth Planet. Inter., 45*, 324-336, 1987.

Isaak, D.G, and E.K. Graham, The elastic properties of an almandine-spessartine garnet and elasticity in the garnet solid solution series, *J. Geophys. Res., 81*, 2483-2489, 1976.

Ito, E., and E. Takahashi, Melting of peridotite at uppermost lower-mantle conditions, *Nature, 328*, 514-517, 1987.

Jeanloz, R., Majorite: Vibrational and compressional properties of a high-pressure phase, *J. Geophys. Res., 86*, 6171-6179, 1981.

Jeanloz, R., Shock wave equation of state and finite strain theory, *J. Geophys. Res., 94*, 5873-5886, 1989.

Jeanloz, R., and T.J. Ahrens, Release adiabat measurements on minerals: The effect of viscosity, *J. Geophys. Res., 84*, 7545-7548, 1979.

Jeanloz, R., and T.J. Ahrens, Equations of state of FeO and CaO, *Geophys. J. Roy. Astron. Soc., 62*, 505-528, 1980.

Jeanloz, R., and R. Grover, Birch-Murnaghan and U_s–U_p equations of state, in *Proceedings of the American Physical Society Topical Conference on Shock Waves in Condensed Matter, Monterey, CA, 1987*, edited by S.C. Schmidt and N.C. Holmes, pp. 69-72, Plenum, New York, 1988.

Jeanloz, R., and E. Knittle, Density and composition of the lower mantle, *Philos. Trans. R. Soc. London, Ser. A, 328*, 377-389, 1989.

Jeanloz, R., and Y. Sato-Sorensen, Hydrostatic compression of $Fe_{1-x}O$ wüstite, *J. Geophys. Res., 91*, 4665-4672, 1986.

Katsura, T., and E. Ito, The system Mg_2SiO_4–Fe_2SiO_4 at high pressures and temperatures: Phase determination of stabilities of olivine, modified spinel, and spinel, *J. Geophys. Res., 94*, 15,663-15,670, 1989.

Kaula, W.M., Thermal evolution of Earth and Moon growing by planetesimal impacts, *J. Geophys. Res., 84*, 999-1008, 1979.

Knittle, E., and R. Jeanloz, Melting curve of $(Mg,Fe)SiO_3$ perovskite to 96 GPa: Evidence for a structural transition in lower mantle melts, *Geophys. Res. Lett., 16*, 421-424, 1989.

Kress, V.C., Q. Williams, and I.S.E. Carmichael, When is a silicate melt not a liquid?, *Geochim. Cosmochim. Acta, 53*, 1687-1692, 1989.

Kumazawa, M., and O.L. Anderson, Elastic moduli, pressure derivatives, and temperature derivatives of single-crystal olivine and single-crystal forsterite, *J. Geophys. Res., 74*, 5961-5972, 1969.

Lange, R.A., and I.S.E. Carmichael, Densities of Na_2O-K_2O-CaO-MgO-FeO-Fe_2O_3-Al_2O_3-TiO_2-SiO_2 liquids: New measurements and derived partial molar properties, *Geochim. Cosmochim. Acta, 51*, 2931-2946, 1987.

Leitner, B.J., D.J. Weidner, and R.C. Liebermann, Elasticity of single crystal pyrope and implications for garnet solid solution series, *Phys. Earth Planet. Inter., 22*, 111-121, 1980.

Levien, L., D.J. Weidner, and C.T. Prewitt, Elasticity of diopside, *Phys. Chem. Miner., 4*, 105-113, 1979*a*.

Levien, L., C.T. Prewitt, and D.J. Weidner, Compression of pyrope, *Am. Mineral., 64*, 805-808, 1979*b*.

Liu, L.-G., Phase transformations and the constitution of the deep mantle, in *The Earth: Its Origin, Structure, and Evolution*, edited by M.W. McElhinny, pp. 177-202, Academic, San Diego, Calif., 1979.

Lyzenga, G.A., T.J. Ahrens, and A.C. Mitchell, Shock temperatures of SiO_2 and their geophysical implications, *J. Geophys. Res., 88*, 2431-2444, 1983.

Manghnani, M.H., R.A. Secco, P. Tao, and T.-C. Liu, Bulk modulus and attenuation in komatiite melts (abstract), *Eos Trans. AGU, 70*, 1369, 1989.

Marsh, S.P., *LASL Shock Hugoniot Data*, 658 pp., University of California Press, Berkeley, 1980.

Matsui, T., and Y. Abe, Formation of a "magma ocean" on the terrestrial planets due to the blanketing effect of an impact-induced atmosphere, *Earth Moon Planets, 34*, 223-230, 1986.

McKenzie, D., The generation and compaction of partially molten rock, *J. Petrol., 25*, 713-765, 1984.

McMillan, P., A Raman spectroscopic study of glasses in the system CaO-MgO-SiO_2, *Am. Mineral., 69*, 645-659, 1984.

McQueen, R.G., S.P. Marsh, J.W. Taylor, J.N. Fritz, and W.J. Carter, The equation of state of solids from shock wave studies, in *High-Velocity Impact Phenomena*, edited by R. Kinslow, pp. 294-417, Academic, San Diego, Calif., 1970.

Miller, G.H., T.J. Ahrens, and E.M. Stolper, The equation of state of molybdenum at 1400°C, *J. Appl. Phys., 63*, 4469-4475, 1988.

Miller, G.H., E.M. Stolper, and T.J. Ahrens, The equation of state of a molten komatiite, 2, Application to komatiite petrogenesis and the Hadean mantle, *J. Geophys. Res.*, this issue.

Nisbet, E.G., The tectonic setting and petrogenesis of komatiites, in *Komatiites*, edited by N.T. Arndt and E.G. Nisbet, pp. 501-522, George Allen and Unwin, Boston, Mass., 1982.

Nisbet, E.G., and D. Walker, Komatiites and the structure of the Archaean mantle, *Earth Planet. Sci. Lett., 60*, 105-113, 1982.

Ohashi, Y., and L.W. Finger, The effects of Ca substitution on the structure of clino-enstatite, *Year Book Carnegie Inst. Washington, 75*, 743-746, 1976.

Ohtani, E., Melting temperature distribution and fractionation in the lower mantle, *Phys. Earth Planet. Inter., 33*, 12-25, 1983.

Ohtani, E., Generation of komatiite magma and gravitational differentiation in the deep upper mantle, *Earth Planet. Sci. Lett., 67*, 261-272, 1984.

Ohtani, E., The primordial terrestrial magma ocean and its implications for stratification of the mantle, *Phys. Earth Planet. Inter., 38*, 70-80, 1985.

Ohtani, E., T. Kato, and H. Sawamoto, Melting of a model chondritic mantle to 20 GPa, *Nature, 322*, 352-353, 1986.

Press, W.H., B.P. Flannery, S.A. Teukolsky, and W.T. Vetterling, *Numerical Recipes in C*, 735 pp., Cambridge University Press, New York, 1988.

Rigden, S.M., T.J. Ahrens, and E.M. Stolper, Densities of liquid silicates at high pressures, *Science, 226*, 1071-1074, 1984.

Rigden, S.M., T.J. Ahrens, and E.M. Stolper, Shock compression of molten silicate: Results for a model basaltic composition, *J. Geophys. Res., 93*, 367-382, 1988.

Rigden, S.M., T.J. Ahrens, and E.M. Stolper, High-pressure equation of state of molten anorthite and diopside, *J. Geophys. Res., 94*, 9508-9522, 1989.

Rivers, M.L., Ultrasonic studies of silicate liquids. Ph.D. dissertation, Univ. of Calif., Berkeley, 1985.

Rivers, M.L., and I.S.E. Carmichael, Ultrasonic studies of silicate melts, *J. Geophys. Res., 92*, 9247-9270, 1987.

Ruoff, A.L., Linear shock-velocity-particle-velocity relationship, *J. Appl. Phys., 38*, 4976-4980, 1967.

Scarfe, C.M., and E. Takahashi, Melting of garnet peridotite to 13 GPa and the early history of the upper mantle, *Nature, 322*, 354-356, 1986.

Shaner, J.W., New ways of looking for phase transitions at multi-megabar dynamic pressures, in *Physics of Solids Under High Pressure*, edited by J.S. Shilling and R.N. Shelton, pp. 99-108, North-Holland, Amsterdam, 1981.

Sparks, R.S.J., P. Meyer, and H. Sigurdsson, Density variation amongst mid-ocean ridge basalts: Implications for magma mixing and the scarcity of primitive lavas, *Earth Planet. Sci. Lett., 46*, 419-430, 1980.

Stebbins, J.F., I.S.E. Carmichael, and L.K. Moret, Heat capacities and entropies of silicate liquids and glasses, *Contrib. Mineral. Petrol., 86*, 131-148, 1984.

Stevenson, D.J., Formation and early evolution of the Earth, in *Mantle Convection*, edited by W.R. Peltier, pp. 873-873, Gordon and Breach, New York, 1989.

Stolper, E.M., and D. Walker, Melt density and the average composition of basalt, *Contrib. Mineral. Petrol., 74*, 7-12, 1980.

Stolper, E.M., D. Walker, B.H. Hager, and J.F. Hayes, Melt segregation from partially molten source regions: The importance of melt density and source region size, *J. Geophys. Res., 86*, 6261-6271, 1981.

Straumanis, M.E., and R.P. Shodhan, Lattice constants, thermal expansion coefficients, and densities of molybdenum and the solubility of sulphur, selenium, and tellurium in it at 1100°C, *Z. Metallkd., 59*, 492-495, 1968.

Swan, G.W., G.E. Duvall, and C.K. Thornhill, On steady wave profiles in solids, *J. Mech. Phys. Solids, 21*, 215-227, 1973.

Swegle, J.W., and D.E. Grady, Shock viscosity and the prediction of shock wave rise times, *J. Appl. Phys., 58*, 692-701, 1985.

Takahashi, E., Melting of a dry peridotite KLB-1 up to 14 GPa: Implications on the origin of peridotitic upper mantle, *J. Geophys. Res., 91*, 9367-9382, 1986.

Takahashi, E., and I. Kushiro, Melting of a dry peridotite at high pressures and basalt magma genesis, *Am. Mineral., 68*, 859-879, 1983.

Takahashi, E., and C.M. Scarfe, Melting of peridotite to 14 GPa and the genesis of komatiite, *Nature, 315*, 566-568, 1985.

Touloukian, Y.S., R.K. Kirby, R.E. Taylor, and P.D. Desai, *Thermal Expansion of Metallic Elements and Alloys*, pp. 208-218, Plenum, New York, 1970.

Walker, D., R.J. Kirkpatrick, and J.F. Hays, Differentiation of komatiitic lava (abstract), *Eos Trans. AGU, 58*, 527, 1977.

Walker, D., C.B. Agee, and Y. Zhang, Fusion curve slope and crystal/liquid buoyancy, *J. Geophys. Res., 93*, 313-323, 6668, 1988.

Walsh, J.M., and R.H. Christian, Equation of state of metals from shock wave measurements, *Phys. Rev., 97*, 1544-1556, 1955.

Watanabe, H. Thermochemical properties of synthetic high-pressure compounds relevant to the Earth's mantle, in *High-Pressure Research in Geophysics*, edited by S. Akimoto and M.H. Manghnani, pp. 441-464, Center for Academic Publishing, Tokyo, 1982.

Wei, K., R.G. Tronnes, and C.M. Scarfe, Phase relations of aluminum-undepleted and aluminum-depleted komatiites at pressures of 4-12 GPa, *J. Geophys. Res., 95*, 15,817-15,827, 1990.

Weidner, D.J., H. Wang, and J. Ito, Elasticity of orthoenstatite, *Phys. Earth Planet. Inter., 17*, P7-P13, 1978.

Weidner, D.J., J.D. Bass, A.E. Ringwood, and W. Sinclair, The single-crystal elastic moduli of stishovite, *J. Geophys. Res., 87*, 4740-4746, 1982.

Williams, Q., P. McMillan, and T.F. Cooney, Vibrational spectra of olivine composition glasses: The Mg-Mn join, *Phys. Chem. Miner., 16*, 352-359, 1989.

Yagi, T., M. Akaogi, O. Shimomura, H. Tamai, and S. Akimoto, High pressure and high temperature equations of state of majorite, in *High-Pressure Research in Mineral Physics*, edited by M. Manghnani and Y. Syono, pp. 141-147, Terra Scientific, Tokyo, 1987.

Zahnle, K.J., J.F. Kasting, and J.B. Pollack, Evolution of a steam atmosphere during Earth's accretion, *Icarus, 74*, 62-97, 1988.

T.J. Ahrens and E.M. Stolper, Division of Geological and Planetary Sciences, California Institute of Technology, Pasadena, CA 91125.

G.H. Miller, Department of Geology and Geophysics, University of California, Berkeley, CA 94720.

(Received March 19, 1990;
revised April 16, 1991;
accepted April 24, 1991.)